AB–INITIO CALCULATIONS OF STRUCTURAL AND ELECTRONIC PROPERTIES OF A $Be_XZn_{1-X}Se$ TERNARY ALLOY

GETASEW MULUALEM ZEWDIE

A THESIS SUBMITTED TO

THE MATERIALS SCIENCE PROGRAM

PRESENTED IN PARTIAL FULFILLMENT OF THE

REQUIREMENTS FOR THE DEGREE OF MASTER OF SCIENCE

(MATERIALS SCIENCE)

ADDIS ABABA UNIVERSITY

ADDIS ABABA, ETHIOPIA

JUNE, 2012

ADDIS ABABA UNIVERSITY

SCHOOL OF GRADUATE STUDIES

This is to certify that the thesis prepared by Getasew Mulualem Zewdie entitled: *Ab–initio Calculations of Structural and Electronic Properties of a* $Be_xZn_{1-x}Se$ *Ternary Alloy* and submitted in partial fulfillment of the requirements for the Degree of Master of Materials Science complies with the regulations of University and meets the accepted standards with respect to originality and quality.

Signed by the Examining Committee:

Examiner: Prof. Teketel Yohannes Signature _____ Date_____

Examiner: Dr. Gebremedhen G/Yesus Signature _____ Date_____

Advisor: Prof. Javed Mazher Signature _____ Date_____

Chair of Department or Graduate Program Coordinator

ABSTRACT

Ab–initio Calculations of Structural and Electronic Properties of a $Be_xZn_{1-x}Se$ Ternary Alloy

Getasew Mulualem Zewdie

Addis Ababa University, 2012

We have used the ab-initio SIESTA code within the framework of DFT, LDA method to calculate the structural and electronic properties of $Be_xZn_{1-x}Se$ alloy for different compositions x = 0.0, 0.33, 0.66, and 1.0. The system is modelled in various possible configurations using a large 54-atom supercell. It is noteworthy to mention that the determination of structural and electronic properties of a $Be_xZn_{1-x}Se$ ternary alloy at x = 0.33 and 0.66 have not been reported earlier to the best of our knowledge. We analyze composition effect on lattice constants, bulk modulus, pressure derivative, bandgap, and density of states. Deviations of the lattice constant from Vegard's law and the bulk modulus from linear concentration dependence are observed. It was deduced that increasing the Be composition in the alloy increases the hardness of the materials. In addition, the calculated band structures showed that the bandgap undergoes a direct-to-indirect transition at the composition of 0.84. The bandgap is found to vary non-linearly with Be composition. Using the approach of Bernard and Zunger, the microscopic origins of bandgap bowing is also explained. It is concluded that the energy bandgap bowing is primarily due to volume deformation effect. Furthermore, the structural phase transformations of ZnSe under high pressure are also studied by similar method. It is found that ZnSe undergoes a first-order phase transition from the zinc blende structure to the rock salt structure at approximately 13.75 GPa. The ground state properties of the phases of ZnSe are also calculated. Our results are in good agreements with experimental observations.

ACKNOWLEDGEMENTS

First, I eulogize the name of Almighty God who gave me power, health, and patience in every endeavor of my life.

I would like to express my genuine and sincere gratitude to my supervisor, Prof. Javed Mazher; his enthusiasm, immense breadth of knowledge, and passion has certainly been infectious and has very much shaped the course of this thesis research. I am forever grateful for his valuable comments; follow up and encouragement while I was working on my thesis research; his time, patience, and interest in my work have never gone unnoticed. Unless and otherwise for unreserved guidance and support, this work would not come to the reality.

I would like to express my sincere feelings to Prof. Teketel Yohannes, Chairman of the Materials Science Program, and Dr. Gebremedhen G/Yesus for their valuable comments and cooperation during this work. My brothers, more than ever Melaku Mulualem, also deserve a special acknowledgment for his significant contributions to this work directly or indirectly.

My heartfelt thanks go to my love, Rahel Mekonnen, for her moral support, encouragement, love, patience and understanding was an immense help throughout my life. I would like to thank also my parents, all the members of my family, especially Mam and Dad, Kelemu M., Ftalew M., Demmelash M., for their unforgettable cooperation in different ways. I cannot afford to forget my friend Eyachew M. without acknowledging him!

I do really want to forward my special thanks to the School of Graduate Studies of AAU and all staff in the Materials Science Program for their help during my study.

TABLE OF CONTENTS

LIST OF FIGURES

LIST OF TABLES

CHAPTER ONE

INTRODUCTION

Recently, there has been increasing interest to study wide bandgap II–VI semiconductors such as ZnSe. Amongst several reasons for this interest, the most prominent is the requirement of these materials for their applications in optoelectronic devices such as light-emitting diodes (LEDs) and laser diodes (LDs) operating in blue-green and UV spectral region. In addition, exploitation of these wide-gap semiconductors holds promise for revolutionary improvements in the cost, size, weight, and performance of a broad range of military and commercial microelectronic and optoelectronic systems [1]. In spite of these lucrative applications, the mechanical properties of ZnSe are much weaker than those of other commonly used semiconductors and the hardness of bulk ZnSe is as low as that of soft metals. This shows that the band structure is not the only important parameter for obtaining viable devices, but that efficient materials design should also involve consideration of the mechanical properties. In this perspective, it has been proposed that alloying ZnSe with a more covalent II–VI compound such as BeSe may significantly alter the mechanical properties and eventually lead to viable defect free devices [2] with longer operating lifetime. In particular, both the mechanical hardness and elastic modulus are expected to be enhanced by increasing the covalency parameter of the new alloys [3]. Since these expectations have not been fulfilled up to now, it is of interest to actually check the influence of BeSe alloying on the crystal properties of ZnSe. As far as we are aware, there is no available experimental or theoretical report on the structural and electronic properties (like; lattice constants, the bulk modulus, pressure derivative of the bulk modulus, bandgap, density of states) and the bowing parameters of a $Be_xZn_{1-x}Se$ alloy especially at beryllium composition (x) values of 0.33 and 0.66.

1.1. Mixed II–VI Semiconductor Alloys

II–VI Semiconductors are the binaries based on one cationic element from group II and one anionic element from group VI, each type being bonded to four nearest neighbors of the other type in an interlocked tetrahedron. The increased amount of charge from group VI to group II atoms tends to cause the bonding to be more ionic than in the case of III–V semiconductors. Representative II–VI semiconductors are ZnS, ZnSe, ZnTe, CdS, CdSe, and CdTe that form either zinc blende or wurtzite lattice structures. Presence of lattice matching has expanded the scope of their device applications beyond those of Si and GaAs [4]. Besides II–VI semiconductor alloys can be created in ternary and quaternary forms, much like the III–V semiconductors. Note that an alloy is a mixture or metallic solid solution composed of two or more elements, especially to give the strength or resistance to the host material. Formation of the substitution alloys usually takes place by atom exchange method, where some of the atoms composing the lattice (host) are substituted with the atoms of the other constituent (dopant). Heavy doping of approximately 50% is required in substitutional alloy for tailoring the mechanical properties. If there are three types of atoms forming the mixture then it is called a ternary alloy.

II–VI wide band gap semiconductors are of high interest for technological applications in fabricating optoelectronic devices [5 – 21]. The possible areas of the device application include laser diodes (LD), light emitting diodes (LED), high-density optical data storage, fiber-optical communication, xerography, underwater measurements, medical imaging, and projection display fabrication. In particular, high–definition and high brightness displays will be directly benefited from the semiconductor laser technology. Additionally, the high ionicity of these compounds

makes them good candidates for high electro-optical and electromechanical coupling [22]. Another popular photoelectronic device is the UV photodetector, which exhibit good response for wavelengths shorter than 400 nm [20]. This is very important for applications that require detection of UV radiation in strong visible and infrared backgrounds. These applications include flame monitoring, heat sensors, UV astronomy, advanced medical instrumentation as well as environmental controlling through biological or chemical reactant detection, ozone monitors, engine control, and pollutant detection. However, the defect formation favored by the highest ionicity and the smallest bond energies of conventional II–VI materials [14] especially in ZnSe family reduces the lifetime of devices in comparison to those based on III–V semiconductors. Perhaps the incorporation of beryllium in II–VI compounds increases the covalence of the alloy and the mechanical resistance of the structures to defect generation and propagation and hence reduces the degradation of the optoelectronic devices [15].

Indeed the compositions of the II–VI semiconductors have demonstrated unique and novel physical properties. For instance these compounds occur in a wide range of various bandgaps and lattice constants influencing the properties of the material. These compounds exhibit the properties like high optical absorption, high mobility, electrical conductivity, and large indices of refraction. At the same time these materials are normally classified according to the type of their bandgap, direct or indirect semiconductors. The direct bandgap semiconductors are found to be advantageous over indirect bandgap semiconductors, as they do not require phonons to satisfy wave vector conservation. Most of the II–VI compounds are found to exist as direct bandgap semiconductors and as a consequence they are dominating the opto-

electronic material for short wavelength applications [23]. Although their alloys are not as well known as those of III–V counterparts, a great deal of effort has been put into improving their properties. Once the band structure parameters of an alloy system have been established, the optical and transport properties can be evaluated by methods familiar from studies on elemental and binary compound semiconductors [24]. For a wide class of materials, $A_xB_{1-x}C$, the value x can be adjusted over a large part of or even the whole concentration range, depending on the miscibility of the alloy system. As the electronic and optical properties vary continuously with x, the electronic properties (e.g. bandgap and thus emission and absorption frequency, dielectric constant, etc.) can be tailored by choosing the appropriate concentration. Therefore, these semiconductor alloys have many applications, not only as bulk semiconductors but also in low-dimensional structures like quantum wells, quantum wires, and quantum dots [25]. The composition variation allows one to obtain intermediate combinations of properties as compared with the properties of the initial end-compounds. The compound alloys find extensive applications in semiconductor devices that require a certain well–defined energy band structure, such as light or electron emitters, detectors, and heterojunction injection lasers.

At present, a strong interest also exists in the II–VI compound solid solutions as well as in the (II–VI)–(III–V) and (II–VI)–(IV–VI) mixtures, mainly in view of the potential that such alloys may hold for extending the bandgap region over which these II–VI compound based systems can be amphoterically doped [26]. In summary, we can say that the wide II–VI semiconductors offer new exciting possibilities for applications in opto-electronic, mobile communication, and cellular automotive. Revolutionary display technology breakthroughs are achieved by them in overhead

illumination, in picture transmission and in visualization techniques along with the short wavelength emitting LD and LEDs. However, some of the best blue-violet color light sources are based on III–V nitrides, but green color presents few difficulties. There are some hopes that ZnSe based structures will be good for such applications [27]. On the contrary, relatively small bond energies and high ionicity of conventional II–VI compounds like ZnSe favour formation of point defects, twins, and dislocations. In fact some progress in this field has already been achieved with use of the alloys containing Be chalcogenides due to a distinctive contribution of covalent bonding and higher cohesive energy of Be compounds which improves mechanical characteristics of II–VI material when Be is substitutionally incorporated to the crystal lattice [14]. It should be noted that besides the predicted increased bond stiffness and the device lifetime, a large difference between energy-gap of constituents (ZnSe and BeSe) and different lattice constants enable controlling the lattice and band parameters of materials in a wide range [28].

1.2. Zinc Selenide Semiconductor

ZnSe is a semiconducting light yellow material which is rarely occurs as a free state in the nature. It can exists in both hexagonal (wurtzite) and cubic (zincblende) crystal structure depending upon the synthesis pressure. The high pressure phase favours the wurtzite structure. ZnSe has high degrees of bond iconicity, polarity, and softness in comparison to other compounds of the II–VI family, thus ZnSe bond length is typical of high value of 2.45 Å [13]. It is an intrinsic n-type wide bandgap II–VI semiconductor with a bandgap of about 2.70 eV at 300 K, in the zinc blende (ZB) structure [29 – 30]. Bulk ZnSe has been extensively studied in relation with different applications as, the fabrication of blue emitting diodes and blue lasers [31 – 34]. In

addition, ZnSe is an attractive material that can be used for the production of various optoelectronic devices for red, blue and green LEDs, LDs, laser screens, thin film transistors, photoelectrochemical cells, solar cells, etc. It is also an optimistic material for windows, lenses, output couplers, beam expanders, and optically controlled switching due to its low absorptivity at infrared wavelength, visible transmission, and giant photo resistivity [34 – 38]. ZnSe-based systems are also promising materials for application in optoelectronic devices operating in the green or yellow spectral regions. Since the first demonstration of ZnSe-based laser diodes (LDs) in 1991, there has been considerable interest concerning LD devices, but the device lifetime is yet to be extended beyond 500 hr [39].

Besides, ZnSe can be substituted for CdS in photovoltaic solar cells and it is also considered as an important photovoltaic material and as a buffer or window material for thin film hetero-junction solar cells. The important properties of photovoltaic interest are the energy bandgap, film thickness, and the wavelength of transmission or absorption of the ZnSe films. In addition to this cadmium is a toxic material and serious effort to substitute the CdS buffer layer by other non-toxic low absorbing materials is required. ZnSe with large direct bandgap (2.7 eV) allows transmission of higher energy photons than the CdS (2.4 eV). The high transmittance increases the potential of ZnSe films for use in the windows material [10]. The bulk ZnSe emission is often dominated by low energy luminescence bands caused by the point defects which introduce energy levels within the bandgap of ZnSe. This is the main problem impeding the development of two dimensional (2-D) ZnSe based laser devices; a high defect density causing generation and propagation of non-radiative recombination defects (dark line defect). However, as dimensions are further reduced, one

dimensional ZnSe structures show properties quite different from that of 2-D structures or bulk materials because of strain relaxation effects. In nanowires with small diameters and large surface area, strain can be easily accommodated, thus inhibiting the formation of misfit dislocations and dark line defects. Another area of difference between bulk ZnSe and ZnSe nanowires has been the dependence of defect density on growth conditions [40]. This size reduction of ZnSe into the nanocrystalline size regime < 9 Å Bohr excitonic radius of ZnSe is another interesting way to remove crystal defects in addition to alloying related modification [41]. The crystal structure of zinc blend ZnSe is shown in Figure 1.1. The structure consists of two inter-penetrating face centered cubic lattices which are displaced by a quarter of the cubic space diagonal.

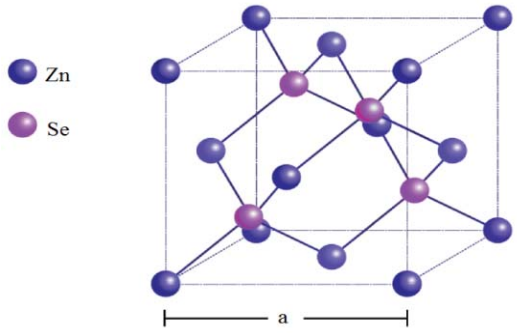

Figure 1.1: The crystal structure of cubic ZnSe.

1.3. Beryllium Selenide Semiconductor

Beryllium (Be) is the chemical element with atomic number four, and at standard temperature and pressure, it is a strong, steel-grey, light-weight, brittle, bivalent alkali earth metal, with a density of 1.85 $g \cdot cm^{-3}$. It also has one of the highest melting points of all the light metals. The Be atom has an ionic radius of 0.45 Å which is nearly a factor of 1.7 times smaller than that of Zn (0.74 Å). The tetrahedral covalent

radius of Be is 0.97 Å, which is about 21% smaller than the tetrahedral covalent radius of Zn (1.22 Å) [13]. Therefore, Be ion finds a lot of vacant space in the ZnSe lattice and settles in a suitable position depending on the various energy minimization process taking place in the lattice for attaining pseudo stabilities, so as to satisfy the Be–Se bond length requirements without actually distorting the Se atom position significantly [41]. BeSe provides interesting aspects for fundamental materials research investigation, because it is characterized by a strong covalent character of chemical bonding, reduced band polarity, short bond length, and large hardness, which are unique among II–VI compounds [42]. The electronic properties of BeSe are characterized by its large bandgap indicate potential device applications for green semiconductor lasers technology. It has been suggested that the optoelectronic devices based on the Be chalcogenides such as BeSe have definite advantage over most of II–VI semiconductors devices due to their high p-type doping concentrations and long lifetimes [27, 43]. Besides, the large bandgap of BeSe suggests the possibility of using these materials for UV optoelectronics [44]. Another interesting feature of BeSe materials is the possibility of lattice matching to Si substrates in the case of $Be_xZn_{1-x}Se$ ternary alloy [14, 45]. Most importantly, the shear modulus of BeSe is larger than the corresponding value for the highly ionic ZnSe.

In fact, the covalent character of BeSe is typically equivalent to that of conventional III–V semiconductors [4]. The extremely small size of Be cations as compared to the anions Se leads to an excess of critical ratio of 4.45 in respect to ionic radii. This implies that these Be compounds are more covalent than the rest of the ionic NaCl type IIA–VI compounds. These inherent differences in the material properties of Be chalcogenides from the rest of the members in the entire IIA–VI series not only make

them ideal candidates for LED and LD operating in the visible region of the spectrum as also in optical disc storage and fiber–optical communication but have also initiated many theoretical and experimental studies [46].

1.4. Comparison of Electronic Properties of ZnSe and BeSe

II–VI binary semiconductors such as ZnSe and BeSe are considered as important technological materials because of their potential applications in optoelectronic devices, solar cells, IR detectors, and lasers [29]. These compound semiconductors are unique within the universe of simple octet compounds, enabling them to dominate higher performance electronics and optoelectronics. One way to think of this uniqueness is of atomic bonding trends that become more polar in moving outwards in the Periodic Table from the column IV semiconductors to the III–V's, II–VI's, and I–VII's [47]. There are two favorable consequences to the polarity trend. Both stem from the tendency, as bonds become polar, for bandgaps to become direct rather than indirect. In other words, electrons at the bottom of the normally unfilled conduction band have the same ($k = 0$) momentum as that of electrons at the top of the normally-filled valence band. The former consequence implies the enhanced photonic absorption from valence electrons and they become conduction electrons, and at the same time conduction electrons emit photons and become valence electrons, without any involvement of phonons that otherwise might be needed to conserve momentum. Thus in comparison to direct materials, the indirect always has a lower radiative recombination coefficient, and is less useful for optoelectronics. Direct have higher radiative recombination coefficients, and thus are more useful for optoelectronics (e.g. ZnSe). And the later consequence implies that the lower electron masses in the direct gap ($k = 0$) electronic states than in that of the indirect gap ($k \neq 0$) electronic states. In

addition, BeSe, which is less ionic, is thus indirect, and has a higher electron effective mass and it is of no use to high-speed electronics; while ZnSe are more ionic, are direct, and have lower electron masses and thus it is more useful for high-speed electronics.

On the contrary, there are also two unfavorable consequences to the polarity trend. First, as bonds become more polar, the greater the energy gained upon transferring electrons between atoms, and the wider the bandgap. This is in addition to another trend, for bandgap to increase with decreasing interatomic spacing between the atoms in the lattice. The closer the atoms are to each other (the smaller the volume per atom), the stronger the covalent bonds, and the larger the bandgap. However, the ionization energies of dopants increase with bandgap, making wider gap semiconductors much more difficult to dope (especially with acceptors to make p–type material) than narrower gap semiconductors. Hence, BeSe, which are less polar, are easy to p–type doping, while ZnSe, which is more polar, is difficult to p–type doping. Second, as the bonds become more polar, their strengths are increasingly determined by electrostatic energies, and depend increasingly less on the angles between bonds. Hence, more–polar semiconductors are less resistant to bond–angle deformation and plastic shear. They are softer materials that more easily incorporate defects such as dislocations. These defects scatter carriers, inhibit photon emission, and enhance device degradation rates.

The band structures for ZB type BeSe and ZnSe are compiled in Figure 1.2 and 1.3, respectively. BeSe have an indirect bandgap with the valence band maximum (VBM) and the conduction band minimum (CBM) occur at the Γ and X, respectively.

Whereas ZnSe have a direct bandgap with the minima of the bandgap located at Γ point. From the band structure curves we may notice the important splitting in the valence bands at the X–point, which is an indication of the importance of the ionicity of the bond as shown in Figure 1.2. This splitting does not exist for the elemental semiconductors such as Si and Ge and it is also small for the III–V semiconductors. But as we can see in Figures 1.2 and 1.3, it is more with low covalency, pronounced for the more ionic systems, which seems to be the case of the II-VI compounds.

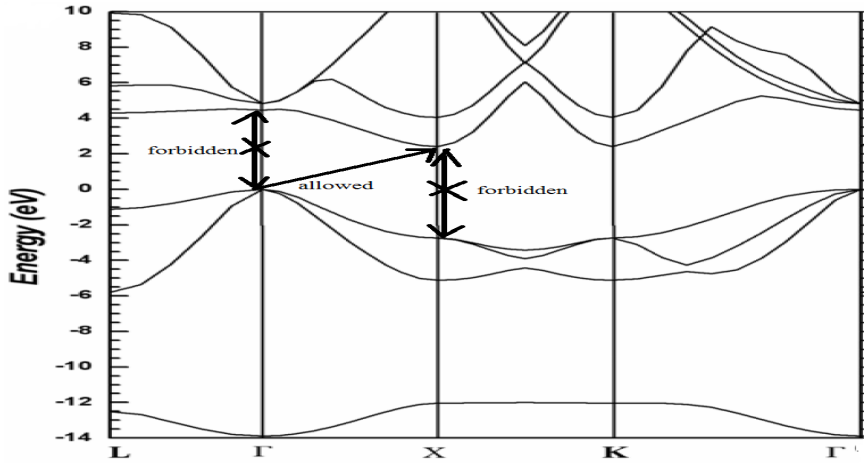

Figure 1.2: The band structure for BeSe [1].

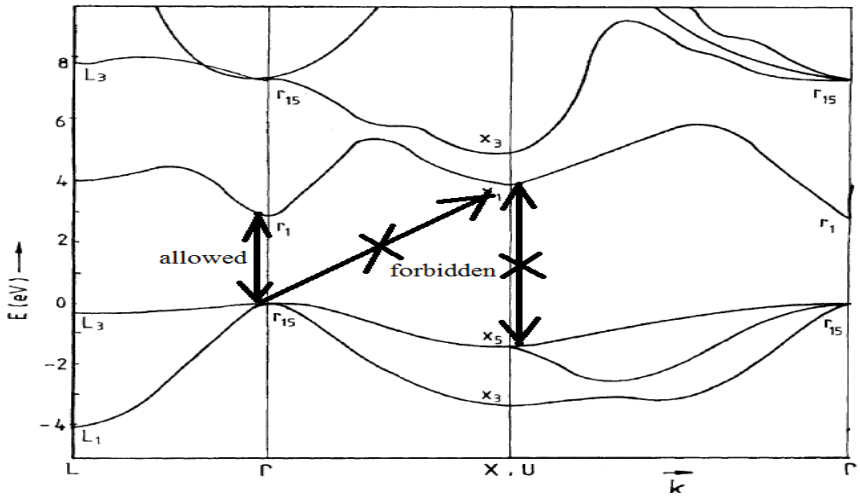

Figure 1.3: The band structure for ZnSe [48].

Nonetheless, among ZnSe and BeSe X split is more apparent in ZnSe due to covalent character of BeSe. Furthermore, we can see that the upper valence energy (marked by arrow) for X point is much lower in comparison to Γ–conduction band minima, which is also indicative of phonon facilited electronic transport process in the BeSe semiconductors.

1.5. Importance of $Be_xZn_{1-x}Se$ Ternary Alloy

The compounds BeSe and ZnSe form a continuous series of alloy ($Be_xZn_{1-x}Se$), where $0 \le x \le 1$ denotes the molar fraction of Be. With both constituents crystallizing in the zinc blende structure, one would expect the properties of the alloy system to vary smoothly between the end points. The compositional variation in a $Be_xZn_{1-x}Se$ alloy induces significant changes in its physical properties such as bond ionicity, electronic band structures and lattice parameter [15]. With increasing value of x, an increasing number of Be atoms replace Zn atoms from the cationic sub lattice sites [12 – 14]. However, in (Be, Zn)Se crystals there is a nearly linear dependence of equilibrium lattice constant with composition, but a relative independence of (average) Be–Se and Zn–Se distances on concentration. When incorporated in a mixed crystal, the individual interatomic distances develop a certain scattering around their mean values, maintaining however, a clear separation between the Be–Se and Zn–Se bond lengths. Specifically, an isolated Be atom may much more efficiently shorten the bonds to Se neighbor whose other three bonds are Zn terminated, than to Se atom shared by other Be neighbors. In particular, a continuous Be–Se chain is characterized by longer link lengths than the average Be–Se distance, for a given concentration [49]. Recently, there is much interest in developing blue-green LD and LEDs and as discussed earlier BeSe is found to be good in replacing ZnSe in the ternary and quaternary alloys [42].

Alloying of BeSe with ZnSe offers an opportunity to create a new family of wide bandgap semiconductors with bandgaps varying from 2.7 to 5.2 eV. The performance and lifetime of the device is depending on the doping material. Doping of Be in ZnSe (i.e. $Be_xZn_{1-x}Se$ ternary alloy) improves the hardness of the host material, which is related to a longer lifetime for devices. The bandgap of $Be_xZn_{1-x}Se$ drops slightly from intermediate concentrations and undergoes a change from direct to indirect character underway from ZnSe to BeSe [50]. A $Be_xZn_{1-x}Se$ alloy is considering the potential of the system for UV detection. Such applications are especially useful when UV light needs to be detected in the presence of substantial visible or infrared backgrounds since these wide gap materials would be solar blind. Potential applications include flame sensors, ozone monitors, plasma diagnostics, and engine control. In general, there are several reasons for particular interest in this alloy [51].

- The potential to integrate the alloy based detectors with Si electronic readouts due to the lattice matching of Si with $Be_xZn_{1-x}Se$. This would permit the fabrication of monolithic detector arrays.
- The greater strength of the $Be_xZn_{1-x}Se$ lattice compared with ZnSe, which is associated with the increased bond covalency. Stacking fault energies are estimated to be considerably higher than those of ZnSe. Stacking faults have been associated with the low lifetimes of ZnSe/GaAs lasers.
- The demonstration of $Be_xZn_{1-x}Se$ epilayers grown by molecular beam epitaxy on Si (001) substrates.
- The report of photodiode quantum efficiencies substantially greater than those of silicon and gallium nitride photodiodes.

Furthermore, $Be_xZn_{1-x}Se$ has a much higher degree of covalent bonding as compared to other (more ionic) wide gap II–VI compounds, which modifies its mechanical properties. This is expected to result in considerable increase of lattice rigidity, a very important factor for reducing defect propagation and therefore increasing the II–VI laser structure lifetime [34, 52]. The lattice constants of $Be_xZn_{1-x}Se$ decreases linearly with increasing x value according to Vegard's rule (i.e. a linear variation of the lattice constant of the alloy *versus* composition x) [15]. It also found that the direct energy gap increases almost linearly with increase of beryllium content [16]. Another very important physical parameter is the thermal diffusivity, which is strongly sensitive to the structure properties of the material. Thermal diffusivity of $Be_xZn_{1-x}Se$ at low temperatures increases about one to two orders of magnitude. The similar temperature variation of thermal diffusivity was found for silicon [52].

1.6. Electronic Properties of a $Be_xZn_{1-x}Se$ alloy

Theoretically, different methods have been used for the calculation of the band structure of a $Be_xZn_{1-x}Se$ alloy using a large supercell of 64 atoms at only x values of 0.25, 0.5 and 0.75; these include methods based on full-potential linear muffin-tin orbital (FP–LMTO) [14], ab-initio full potential linearized augmented plane wave (FP–LAPW) method [15], self-consistent pseudopotential [16], virtual crystal approximation and empirical pseudo-potentials [51]. Their results show a direct bandgap at Γ point for ZnSe and $Be_xZn_{1-x}Se$, the indirect bandgap character of BeSe is commonly accepted and so there must be a direct to indirect transition when x vary from 0 to 1 in $Be_xZn_{1-x}Se$ (see Figure 1.5). And also a crossover between the direct and indirect bandgaps of $Be_xZn_{1-x}Se$ is observed at the composition (x) of 0.79 [15]. The fundamental gap ($E_{\Gamma-\Gamma}$) increases with the concentration (x). The direct (Γ–Γ) and

indirect (Γ–X) gaps of $Be_xZn_{1-x}Se$ are plotted as a function of x in Figure 1.5, and the lowest indirect gap is found to be always Γ–X transition.

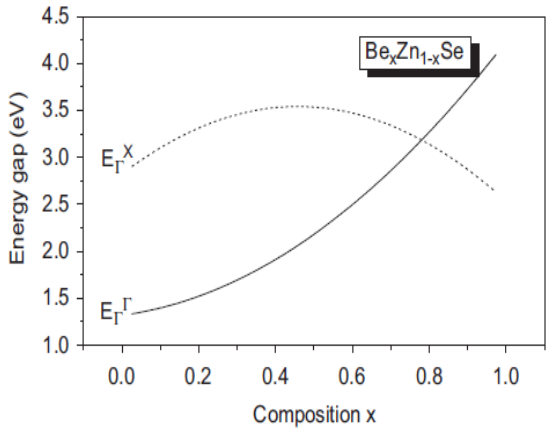

Figure 1.4: Composition dependence of the direct (Γ–Γ) and indirect (Γ–X) bandgaps in a $Be_xZn_{1-x}Se$ alloy [14].

The lattice constant varies linearly with the composition x according to the so-called Vegard's law [14, 16, 27, 53, 54, 55].

$$a(A_xB_{1-x}C) = xa_{AC} + (1-x)a_{BC} \qquad (1.1)$$

Where a_{AC} and a_{BC} are the equilibrium lattice constants of the binary compounds AC and BC, respectively, and $a(A_xB_{1-x}C)$ is the alloy lattice constant. However, deviation from the pure mean field theoretical studied of the Vegard's law has been observed in the semiconductor alloys both experimentally and by ab-initio techniques. Hence, the lattice constant predicted by Vegard's method can be written as

$$a(A_xB_{1-x}C) = xa_{AC} + (1-x)a_{BC} - x(1-x)b \qquad (1.2)$$

Where the quadratic term 'b' is the bowing parameter, the composition dependence of the bandgap is described by a second-order polynomial with the quadratic term proportional to the so-called bowing parameter (b) so that

$$E_g(x) = xE_{BC}(a_{BC}) + (1-x)E_{AC}(a_{AC}) - bx(1-x) \qquad (1.3)$$

The physical origins of the gap bowing (bending of the bandgap) in a $Be_xZn_{1-x}Se$ alloy is calculated following the procedure of Bernard and Zunger [14, 27, 54], in which the bowing parameter (b) is decomposed into three physically distinct contributions resulting from volume deformation, charge exchange, and structural relaxation. The overall bowing coefficient measures the change in various physical properties according to the following reaction

$$xBeSe(a_{BeSe}) + (1-x)ZnSe(a_{ZnSe}) \rightarrow Be_xZn_{1-x}Se(a_{eq}) \qquad (1.4)$$

Where, a_{BeSe} and a_{ZnSe} are the equilibrium lattice constants of the binary compounds BeSe and ZnSe, respectively and a_{eq} is the equilibrium lattice constant of the alloy at the average composition x. The different contributions to the bandgap bowing 'b' can be mainly attributed to the following three factors. The first factor measures the effect of volume deformation (VD) on the bowing. The corresponding contribution to the gap bowing parameter 'b_{VD}' represents the relative response of the band structures of the ternary BeZnSe to its hydrostatic pressure, which usually arises from the change of their individual equilibrium lattice constants of the binaries ZnSe and BeSe in respect to their ternary alloy value a = a(x) as calculated from Vegard's rule, according to the following reaction:

$$BeSe(a_{BeSe}) + ZnSe(a_{ZnSe}) \rightarrow BeSe(a) + ZnSe(a) \qquad (1.5)$$

So that

$$b_{VD} = \frac{E_{BeSe}(a_{BeSe}) - E_{BeSe}(a)}{1-x} + \frac{E_{ZnSe}(a_{ZnSe}) - E_{ZnSe}(a)}{x} \qquad (1.6)$$

The second contribution, the charge exchange (CE) contribution 'b_{CE}' reflects a charge transfer effect which is due to the different (averaged) bonding behavior at the lattice constant 'a'. The formal reaction is

$$xBeSe(a) + (1-x)ZnSe(a) \rightarrow Be_xZn_{1-x}Se(a) \qquad (1.7)$$

The contribution of this structural relaxation to the bowing is hence

$$b_{CE} = \frac{E_{BeSe}(a)}{1-x} + \frac{E_{ZnSe}(a)}{x} - \frac{E_{Be_xZn_{1-x}Se}(a)}{x(1-x)} \qquad (1.8)$$

The final step measures *via* parameter by 'b_{SR}' changes due to the structural relaxation (SR) in passing from the unrelaxed to the relaxed alloy.

$$Be_xZn_{1-x}Se(a) \rightarrow Be_xZn_{1-x}Se(a_{eq}) \qquad (1.9)$$

$$b_{SR} = \frac{E_{Be_xZn_{1-x}Se}(a) - E_{Be_xZn_{1-x}Se}(a_{eq})}{x(1-x)} \qquad (1.10)$$

All these energy gaps occurring in expressions 1.6, 1.8, and 1.10 have been calculated for the indicated atomic structures and lattice constants. Consequently, the total gap bowing parameter is defined as $b_{VD} + b_{CE} + b_{SR}$.

1.7. Effect of Pressure on General Properties of Materials

As a matter of fact the materials science is all about probing the properties of either already existing materials, or designing new ones, in the said context we noticed that pressure, along with temperature, are extremely important, powerful, and flexible levers for such purposes. It allows squeezing atoms (or molecules) closer, overcome energy barriers, which might be too high at ambient conditions, and force the materials into new crystallographic arrangements. Employed together with temperature, pressure allows exploring phase diagrams in a systematic way, hunting for peculiar structures and unusual atom co-ordinations. When it comes to the study of alloys, the concentration behaves as an additional variable spanning the space of possible phases. In fact, chemical doping and external pressure have exhibited in some cases similar, and in other complementary effects, as they both assist in producing internal stress, which might only be relieved through a structural

transformation in a confined system. The fascinating thing about the effect of pressure is that it does not affect individual atoms directly, in a universally predictable way, hence the variety of phase transformations exist in the materials, which might seem only minutely different in their electronic structures.

Application of pressure can induce a crystalline phase change in the material for attaining the stability maxima. As the phase-change material is confined in a closed space, significant mechanical stress is developed in the material, and the most natural way for the stress relaxation is the phase transition from lower coordination to higher. Furthermore it is found that phase transition inevitably affects the electrical properties of the material. The compressive stress induced transition increases the conductivity of the materials by reducing the energy gap and creating in-gap states. Also it is found that the resistance declines monotonically with the application of hydrostatic pressure at room temperature, in many chalcogenide semiconductors the energy gap decreases as the pressure increases, or $dE_g/dP < 0$. Therefore, the compressive stress reduces the resistivity by reducing the electronic bandgap [56]. The study of phase transitions under pressure is not only of interest for practical materials research, but it offers a rich playground in physics, basic electronic structure theory, lattice dynamics, and transport. Electronic properties exhibit effects of the extent of localization and the lattice vibrations are indicating to a kinetic way of understanding the origin of the new phase. Pressure also plays a key role in determining the thermodynamics of the materials. It affects overall interatomic and intermolecular distances and hence the density. The variation of interatomic distances allows scanning of atomic and molecular interactions and thus revealing exotic structural, electronic, optical, elastic, and thermal properties.

Actually, now adays, the field of study of matters under high pressure is no more restricted to hard physical science; it has extended to affect our immediate needs or daily life interest, ranging from commercial treatment of foodstuffs to investigating the origins of life. Among diverse interests in high–pressure science, there is a quest for achieving new or exotic properties that do not exist at the ambient pressure. Interestingly enough, a high-pressure phase that may be enforced under high pressure exists sometimes as a metastable phase at the ambient pressure. The most remarkable example of this is probably made by diamond, which is a metastable phase of carbon at ambient conditions, the ground-state phase being graphite. Pressure is capable to drastically redistribute electron density, thus changing the nature of chemical bonds and converting insulators into metals (including hydrogen) and soft bonds into stiff ones [57]. Elastic properties of solid are also important due to fundamental solid-state phenomena such as equation of state, phonon spectra, and atomic potentials. Elastic stiffness coefficients are essential for many applications related to mechanical properties of a solid such as internal strain, thermo-elastic stress, and load deflection. The extent of the deformations is depending on elastic stiffness coefficients that is a very important characterization of the crystals under varying pressure. Moreover, the elastic constants of the materials at high pressures are essential in order to predict and understand material response, strength, mechanical stability, and phase transitions [58].

1.8. Murnaghan Equation of State

Francis D. Murnaghan of John Hopkins University developed the Murnaghan Equation of state [59 – 61] for the calculation of elastic constants of the material like bulk modulii with the help of pressure response and now a day this equation is widely

used for the calculation of applied pressure with the help of changes in structural volumes during phase transitions. He presented an equation of state suitable for representing solids. It is to be noted that volume and total energy have interdependence and thus the equation of state has found considerable use in the condensed phase media. Three derivative relations are mostly utilized to lead to the final formulation, namely:

$$P = -\left(\frac{\partial E}{\partial V}\right)_S \tag{1.11}$$

$$B = -V\left(\frac{\partial P}{\partial V}\right)_T \tag{1.12}$$

$$B' = \left(\frac{\partial B}{\partial P}\right)_T \tag{1.13}$$

Where P is the pressure, E is the internal energy, V is the volume, B is the bulk modulus, and B' is the pressure derivative of the bulk modulus at constant temperature. Making the assumption that B' is a constant allows one to assign a linear dependence of the bulk modulus on the pressure, which allows specifying the single bulk modulus as a variant, while the derivative (B') represented as the materials constant. This leads to a relationship for pressure:

$$P = \frac{B}{B'}\left[\left(\frac{V_0}{V}\right)^{B'} - 1\right] \tag{1.14}$$

That can be integrated to represent the change in the energy of the solid with respect to the elastic constants or the pressure.

$$E(V) - E(V_0) = \frac{BV}{B'}\left[\frac{\left(V_0 / V\right)^{B'}}{B'-1} + 1\right] - \frac{BV_0}{B'-1} \tag{1.15}$$

Where, E(V) is the total energy at cell volume V, $E(V_0)$ is the total energy at equilibrium volume V_0 (at P = 0). In the present work, the elastic constants of the alloy have been calculated by Equation 1.15 of the Murnaghan Equation of state. For a given equation of state (EOS), which expresses the energy 'E' as a function of the lattice parameter 'a' or volume 'V' the bulk modulus 'B' can also defined by Equation 1.16 [62].

$$B = V\frac{\partial^2 E}{\partial V^2} = \frac{4}{9a}\frac{\partial^2 E}{\partial a^2} \tag{1.16}$$

The unit cell volume 'V' is calculated simply by V = abc for orthorhombic and V = a^2c for tetragonal structures, where a, b, c are lattice parameters [63]. But for a FCC lattice the volume is (1/4) a^3 [62], because, four of each atom are present in a unit cell of ZB (FCC) crystal structure, for e.g. for ZnSe each Zn atom is surrounded by four equi-distant Se atoms, at the corners of a regular tetrahedron, similarly each Se atom is surrounded tetrahedrally by four Zn atoms. The values of estimated B can further be used to study the variation of the unit cell volume V/V_0 with pressure P by using the Murnaghan's Equation of state given as [63]

$$\frac{V}{V_0} = \exp\left[-\frac{1}{B'}\ln\left(1+\frac{B'}{B}\left(P-P_0\right)\right)\right] \tag{1.17}$$

Where, P_0 is the ambient or initial pressure. In general, the Murnaghan Equation of state breaks down for compression ratios greater than ~ 0.7 – 0.8 times the original volume, which occurs as a consequence of the triggering nonlinear dependence of the bulk modulus on pressure and variability of bulk modulus pressure derivative at higher pressures. Nevertheless, the bulk modulus is an important physical parameter of crystals; it reflects bonding characters in crystals and, in many instances it is used as an indicator for crystal strength and hardness. A number of researchers have focused upon the bulk modulus in their search for new super–hard materials because

the hardness correlates roughly with the bulk modulus for group IV, III–V, and II–VI materials; the bulk modulus results can be extensively used to predict the hardness of a new material [64].

1.9. Pressure Effect on Structural Properties of a $Be_xZn_{1-x}Se$ alloy

The fundamental nature and technological importance of the elemental and binary semiconductors have made their high-pressure behavior, one of the most active areas of high-pressure research since the advent of the diamond–anvil cell (DAC) over 30 years ago [65]. Since then, this subject has attracted a lot of attention. Not too long ago the general accepted view of II–VI compounds are considered as the compounds which transform under high pressure from the zinc blende (ZB) or wurtzite to the rock salt (RS) and then to the β-Sn phases, with the exception of the Hg-based compounds. In the latter compounds, the cinnabar phase (which is the ground state structure of HgS) appears before RS. However, recent experiments performed by using angle-dispersive X-ray techniques for many II–VI, III–V, and group–IV semiconductors have altered significantly their widely accepted structural perception [66]. For instance, the $Be_xZn_{1-x}Se$ amid system, the constituent components ZnSe, BeSe exhibit contrasting properties, and their pressure induced phase transformations also follow different paths. Pure ZnSe and BeSe both crystallize in the ZB structure at low pressure and are known to transform cubic rock salt (NaCl) and hexagonal NiAs structure, respectively, at high pressure. BeSe remain semiconductors in the high-pressure NiAs phase, like the II–VI ionic ZnSe [10, 67]. For these alloy materials, one can treat the ZB phase as the ambient pressure phase for all the compounds considered due to their stability and their polymorphic structural transformation.

Besides, ZB has fewer atoms per unit cell, and is therefore computationally easier to treat [68].

In summary, the application of an external hydrostatic pressure to materials will certainly lead to shrinkage in volume and the total free energy of the system will also be affected from the thermodynamic criterion of equilibrium [69]. In the $Be_xZn_{1-x}Se$ system the phase transformation pressure increases linearly with x. When Be concentration is increased, the lattice becomes more BeSe like and the Zn–Se bonds are under compression when compared to pure ZnSe. The lattice dynamics of the BeZnSe crystal basically changes when approaching the ZB→RS ZnSe-like transition under pressure, which is an unnatural transition for the Be-Se bonds. The basic trend is that the ZB→RS transition is regularly shifted to higher pressure when the incorporation of Be increases. This is due to the reinforcement of the highly ionic (soft) ZnSe lattice by the strongly covalent (stiff) Be-Se bonds. Besides, the X-ray diffraction data indicate that the ZB→RS transition is very sharp, and that the crystal adopts the RS structure as a whole [16]. Hence it would be interesting to explore the structure and electronic properties of ZBs alloy at different novel compositions. Especially a general trend of change in elastic constant with change in pressure and phases, as well as its effect on bandgap bowing are much needed to be explored in detail.

CHAPTER TWO

OBJECTIVES

2.1. General Objectives

To Study the structural and electronic properties of a $Be_xZn_{1-x}Se$ ternary alloy using ab-initio (first principle) techniques.

2.2. Specific Objectives

- To prepare simulation samples for compositionally varied $Be_xZn_{1-x}Se$ at Be composition (x) of 0.0, 0.33, 0.66, and 1.0 using ab-initio SIESTA code.
- To study the modeled substitutionally doped $Be_xZn_{1-x}Se$ alloy.
- Use ab-initio DFT-LDA approach for exploring the variations in structural and electronic properties (like; lattice constants, the bulk modulus, pressure derivative, bandgap, and density of states) and the bowing parameters with respect to compositional-phase variation on ternary alloy of $Be_xZn_{1-x}Se$.
- Use ab-initio DFT-LDA approach to predict the Pressure Effect on Structural Properties of ZnSe.

CHAPTER THREE

METHODOLOGIES AND SIMULATIONS

3.1. Basics of Theory and Approximations used

3.1.1. Ab–initio (first principle) techniques for many-body treatment

As the accuracy becomes more and more important in computational research, there is a strong need for using Ab-initio (first-principles) based methods for studying electronic structures of large systems [70]. In these kinds of calculations, only the atomic number and the number of the atoms are used as an input for the calculations. Most existing ab-initio methods for the numerical calculation of the electronic properties of solids are based on density functional theory (DFT). But as the functional dependence of the kinetic energy and the exchange and correlation part of the Coulomb (interaction) energy on the electron density is not known explicitly, additional approximations are necessary. Here the most common and successful method is the local density approximation (LDA), which assumes that the exchange-correlation potential depends locally on the electronic density. Such DFT-LDA calculations have been very successful for many materials and ground-state properties such as crystal structure, ground state and ionization energy, lattice constant, etc. [71].

All first principles, quantum mechanical or ab-initio, methods require a solution to the many-particle Schrödinger Equation. The exact solution of the full many-bodied Schrödinger equation describing a material is difficult to achieve by contemporary computational skills, but by using a series of approximations, the electronic structure and so the total energy of most materials can be calculated quite accurately. The total energy of a compound is defined as the energy required to bring all constituent

electrons and nuclei together from infinite distance, where they do not interact to form an aggregate [72]. A solid is a collection of heavy, positively charged particles (nuclei), if the structure is composed of N nuclei and each has Z electrons, then it has N (nuclei) + ZN (electrons) as the electromagnetically interacting particles. This is known as a many-body problem, and total number of these particles are so light that these can be compared with classical particles thus it becomes quantum many body problem. In principle, to study the materials and their properties, we have to solve the time independent Schrödinger Equation give by

$$\hat{H}\Psi = E\Psi \tag{3.1}$$

Where $$\hat{H} = T_n + T_e + V_{en} + V_{ee} + V_{nn} \tag{3.2}$$

$$\hat{H} = -\frac{\hbar^2}{2}\sum_i \frac{\nabla_{Ri}^2}{M_i} - \frac{\hbar^2}{2}\sum_i \frac{\nabla_{ri}^2}{m_e} - \frac{1}{4\pi\varepsilon_0}\sum_{i,j}\frac{e^2 Z_i}{\left|R_i - r_j\right|} + \frac{1}{8\pi\varepsilon_0}\sum_{i\neq j}\frac{e^2}{\left|r_i - r_j\right|} + \frac{1}{8\pi\varepsilon_0}\sum_{i\neq j}\frac{e^2 Z_i Z_j}{\left|R_i - r_j\right|} \tag{3.3}$$

Here Ψ, is the wave function of all participating particles and H is the exact many-particle Hamiltonian for this system. The first term in Equation (3.3) is the kinetic energy operator for the nuclei (T_n), the second for the electrons (T_e). The third term corresponds to Coulomb electron-nuclear attraction (V_{en}), the fourth term for electron-electron repulsion (V_{ee}) and the final term for nuclear-nuclear repulsion (V_{nn}), respectively. Also, M_i is the mass of the nucleus at R_i, m_e is the mass of the electron at r_i. In order to find acceptable approximate eigen states (acceptable solution to Schrödinger Equation (3.1)), Born-Oppenheimer approximation [73] can be used. These approximations make the calculations easy to transform the many body problem to one body problem.

3.1.1.1. The Born-Oppenheimer approximation

The Born-Oppenheimer approximation is one of the most important approximations in materials science. The special idea of the approximation is that the nuclei are much heavier and much slower than the electrons. We can hence freeze them at fixed positions and thus assume the electrons to be in instantaneous equilibrium with them. This mean that only the electrons are kept as key players of the many body problem while nuclei are deprived from this status, and reduced merely to sources of positive charges; they become external to the electron cloud. The application of this approximation manifests by a collection of ZN interacting negative particles, moving in the potential of the nuclei in the given problem. So consequently of the Born-Oppenheimer approximation predicts that the Hamiltonian of the nuclei do not move any more, their kinetic energy is zero and the first term in Equation (3.2) disappears and the last term reduces to a constant. Therefore the many body problem is left with the kinetic energy of the electron gas, the potential energy due to electron- electron interactions and the potential energy of the electrons in the potential of the nuclei. The new many body Hamiltonian is written formally as

$$\hat{H} = -\frac{\hbar^2}{2}\sum_i \frac{\nabla_{ri}^2}{m_e} + \frac{1}{8\pi\varepsilon_0}\sum_{i\neq j}\frac{e^2}{\left|r_i - r_j\right|} - \frac{1}{4\pi\varepsilon_0}\sum_{i,j}\frac{e^2 Z_i}{\left|R_i - r_j\right|}$$

or

$$\hat{H} = T_e + V_{ee} + V_{en} \qquad (3.4)$$

3.1.2. Density Functional Theory

In modeling either atomic or molecular systems, the most common strategy relies on approximate solutions of Schrödinger Equation; and the so-called density functional theory (DFT) has been established as one of the most widely used first-principles

methods in many fields. DFT theory is first realized by Thomas and Fermi [74] by the proposition of the electronic structure of solids in their ground states that is fully treated in terms of the electron density (ρ) alone. Hohenberg and Kohn [75] later formalized this fact by giving the origin to the DFT. The quantum many body problem obtained after the first level approximation (Born-Oppenheimer) is much simpler than the original one, but still difficult to solve. To reduce Equation 3.4 to an approximate but acceptable form, the Hartree-Fock method (HF) is used. In this approximation [76], the solution of many-electron Hamiltonian is transformed to solve one-electron Hamiltonian by assuming the electrons are independent from each other. By this assumption the total wave function for the electrons is written as

$$\Psi\left(r_1, r_2, \ldots\ldots\ldots \quad .r_N\right) = \prod_i^N \psi(r_i) \tag{3.5}$$

Where (Ψ) is the electron wave function, using this definition the electron density is

$$\rho(r) = \sum_i^N \left|\psi_i(r)\right|^2 \tag{3.6}$$

Where $\rho(r)$ is the electron density, the total Hamiltonian can be written

$$\hat{H} = -\frac{\hbar^2}{2}\sum_i \nabla_{ri}^2 - \frac{1}{4\pi\varepsilon_0}\sum_i \sum_j \int \frac{eZ_j \left|\psi(r_i)\right|^2 d^3 r_i}{\left|R_j - r_i\right|} + \frac{1}{8\pi\varepsilon_0}\sum_i \sum_j \frac{\left|\psi(r_i)\right|^2 \left|\psi(r_j)\right|^2 d^3 r_j d^3 r_i}{\left|r_i - r_j\right|}$$

or
$$\hat{H} = T_0 + V_H(\psi) \tag{3.7}$$

The Schrödinger Equation becomes non-linear and requires for the self-consistency procedure.

$$\left[T_0 + V_H(\psi)\right]\Psi = E_H \Psi \tag{3.8}$$

Here, T_0 is the functional for the kinetic energy of a non-interacting electron gas; V_H stands for the electron effective potential and E_H is the functional of electron energy using Hartree-Fock approximation. In order to solve an equation of this type, one

starts with some trivial solution $\Psi^{(0)}$ (normally atomic orbital wave function is used) which is used to construct the potential. Solving the non-linear Schrödinger Equation, Equation 3.8, with this potential one can obtain a new solution $\Psi^{(1)}$, which is used in turn to build a new potential, the ab-initio techniques for atomic potential generation are also referred as pseudopotential methods. This procedure is repeated until the ground state $\Psi^{(i)}$ and the corresponding energy 'E' do not deviate appreciably from those in the previous step. Hartree-Fock approximation performs very well for atoms and molecules, and therefore used a lot in quantum chemistry. For solids, it is less accurate, however. In the present work, the electronic band structure of the compounds and their alloy has been studied by DFT, which is more modern and probably more powerful compared to HF approximation. DFT formally established by the two ground breaking theorems due to Hohenberg and Kohn [75].

3.1.2.1. The Theorems of Hohenberg and Kohn

Hohenberg and Kohn (HK) proposed the DFT approach based on the following two theorems:

First theorem: The ground-state energy of a many-body system is a unique functional of the particle density, $E_0 = E[(\vec{r})]$. In other word there is one-to-one correspondence between ground state density of a many electron system (atom, molecule, solid) and the external potential V_{ext}.

Second theorem: The functional $E[(\vec{r})]$ has a minimum when evaluated with the exact ground-state energy (The ground state is assumed to be degenerate). The ground-state energy functional is written as:

$$E[\rho] = \int \rho(r) V_{ext} dr + F_{HK}(\rho) \qquad (3.9)$$

Where V_{ext} is the external potential, i.e., the potential due to the nuclei–electron attraction and F_{HK} is the Hohenberg–Kohn functional, which includes contributions due to the kinetic energy of the electrons and the electron–electron repulsion. Using the above energy functional, along with the constraint that the volume integral of the electron density yields the total number of electrons, N, we extremalize the functional to derive the ground-state energy of the system. The resulting ground-state energy is given by

$$\mu = \frac{\delta E[\rho]}{\delta \rho(r)} = V_{ext} + \frac{\delta F_{HK}[\rho]}{\delta \rho(r)} \tag{3.10}$$

Where 'μ' is the Lagrange multiplier introduced in order to satisfy the electron density constraint. The two HK theorems, thereby, prove that the ground-state electron density contains all the information about the ground-state energy, which is required to determine all the states of the system. The absence of an exact expression for the kinetic energy functional precludes the analytical solution of Equation 3.10. To accurately determine the ground-state energy, Kohn and Sham developed a procedure for an effective single-particle Hamiltonian that results in one-particle equations (drawing an analogy with the Hartree–Fock method).

3.1.2.2. The Kohn–Sham Scheme

Furthermore, Kohn and Sham proposed that the many-electron system can be replaced by a fictitious non-interacting many particle system with the same external potential, all the interactions between electrons are classified into an exchange correlation (XC) term. The theorem of Kohn and Sham [77] can be formulated in terms of the exact ground-state density $\rho(r)$ of an N-electron system given by:

$$\rho(r) = \sum_{i}^{N} \Psi_i^*(r)\Psi_i(r) \tag{3.11}$$

Where, the single-particle wave functions $\Psi_i(r)$ are the N lowest energy solutions of the Kohn-Sham equation

$$H_{KS}\Psi_i = E_i\Psi_i \qquad (3.12)$$

To find the ground-state density, we do not need to use the second Hohenberg-Kohn theorem any more, but we can rely on solving the familiar Schrodinger (like non-interacting single particle) equations. But be aware that the single-particle wave functions '$\Psi_i(r)$' are not the wave functions of electrons; they describe mathematical quasi-particles, without a direct physical meaning. Only the overall density of these quasi-particles is used to be equal to the true electron density. Besides the single particle energies, E_i are also not single-electron energies. Both the Hartree operator V_H and the exchange-correlation operator V_{xc} depend on the density $\rho(r)$, which in turn depends on the $\Psi_i(r)$, which are being searched. Some starting density $\rho^{(0)}$ is guessed, and a Hamiltonian H_{KS1} is constructed with it. The eigenvalue problem is solved, and results in a set of Ψ_i from which a density ρ_1 can be derived. Most probably ρ^0 will differ from ρ_1. Now ρ_1 is used to construct H_{KS2}, which will yield a ρ_2, etc. The procedure can be set up self consistently in such a way that this series will converge to a density ρ_f, which generates a H_{KSf}, which again yields a solution ρ_f, this converged final density is then consistent with the Hamiltonian.

3.1.3. The Exchange–Correlation Functional

The Kohn-Sham scheme described above is exact in nature in comparison to the preceding Born-Oppenheimer approximation, and thus further approximations are now required. However, we neglected so far the fact that we do not know the

exchange–correlation (XC) functional. A widely used approximation called the Local Density Approximation (LDA) [78] is used to postulate that the exchange-correlation functional and it has the following form

$$E_{XC}^{LDA} = \int \rho(\vec{r}) \in_{XC} (\rho(\vec{r}))d\vec{r} \tag{3.13}$$

Where $\in_{XC} (\rho(\vec{r}))$ is the exchange-correlation energy density of a homogeneous gas with density $\rho(r)$, and $\in_{XC}$ can be expressed by two terms, which are exchange and correlation contributions, given by the following form

$$\in_{XC} \left(\rho(\vec{r})\right) = \in_{X} \left(\rho(\vec{r})\right) + \in_{C} \left(\rho(\vec{r})\right) \tag{3.14}$$

$\in_{X} (\rho(\vec{r}))$, is the exchange energy for the one electron in the uniform electron gas with the density $\rho(\vec{r})$ and is given by the Dirac form

$$\in_{X} (\rho(\vec{r})) = -\frac{3}{4}\sqrt[3]{\frac{3\rho(\vec{r})}{\pi}} \tag{3.15}$$

Nevertheless, there exist a number of different approximations for the exchange correlation energy. The exchange-correlation potential is the functional derivative of the exchange-correlation energy, and is a mean-field quantum mechanical interaction potential between the electrons [78].

$$V_{XC}[\rho](r) = \frac{\delta E_{XC}(r)}{\delta \rho(r)} \tag{3.16}$$

Thus the total energy is a functional of the electron density ρ and it is given by

$$E[\rho] = T[\rho] + E_{XC}[\rho] + E_{H}[\rho] + E_{ext}[\rho] \tag{3.17}$$

Where $T[\rho]$, is the kinetic energy of the Kohn-Sham orbitals, E_{XC} is is the exchange-correlation energy, $E_{H}[\rho]$ is the Hartree energy and $E_{ext}[\rho]$ is the interaction energy with the pseudo potential ions and other electro-static external potentials. The forces

(F_i) are calculated by differentiating the total energy with respect to the ionic coordinate of atom (i) at position (R_i)

$$F_i = \frac{dE[\rho]}{dR_i} \tag{3.18}$$

At the same time Equation 3.18 also demarcates an important procedure of the geometrical optimization in the aid of DFT. Thus the XC term is an important part in the density functional calculation and we cannot do any practical calculation without knowing an approximate form of this term.

3.2. Methodology for Atomistic Simulations

3.2.1. SIESTA

SIESTA (Spanish Initiative for Electronic Simulations with Thousands of Atoms) is both a method and computer program implementations, to perform electronic structure calculations and ab-initio molecular dynamics simulation of molecules and solids. It is a numerical implementation of DFT constructed on a non-orthogonal localized atomic orbital basis set. SIESTA also solves problems at the level of DFT; these problems are, generally, related to ground-state properties. Energy/volume curves, phase diagrams (e.g., magnetic ones), phonons, molecular dynamics are all related to ground-state properties [79]. Some characteristics of SIESTA are:

- It uses the standard Kohn-Sham self-consistent density functional method in the LDA or generalized gradient approximation (GGA).
- It uses atomic orbitals as a basis set, allowing unlimited multiple-zeta and angular momenta, polarization and off-site orbitals.
- Projects the electron wave functions and density onto a real-space grid in order to calculate the Hartree and XC potentials and their matrix elements.

3.2.2. Atomistix Software Package

Quantum Wise provides two different interfaces for performing electronic transport calculations: Virtual NanoLab (VNL), which is a graphical user interface (GUI), and Atomistic Toolkit (ATK), which is a file-based or command line interface. However, which of the interfaces to use, is sometimes a matter of taste, and sometimes determined by the task at hand. Most users will probably find that VNL is the most appealing option, because of its intuitive ease of use. Some prefer ATK because it is more transparent, gives more control and calculations can be automated by using scripts. Generally, ATK/VNL is designed for electronic transport calculations based on DFT and local basis set. The strength of ATK and VNL lies in their flexibility to describe systems of different symmetries [80 – 81].

3.2.2.1. Atomistix Toolkit

ATK is a library of atomic scale modeling techniques that can be used to calculate a wide range of properties of nanoscale systems. The most unique features are the ability to calculate the electrical properties of nanoscale devices, which consist of a scattering region coupled to two macroscopic bulk systems or electrodes. The systems may contain nanowires, nanotubes, graphene, high-k dielectric interfaces, semiconductors, metals, etc. A modelling study generally consists of three parts: setting up the calculation, running the calculation, and finally analyzing the output of the calculation. Once the system to be studied is defined, the method of calculation must be specified. The description of the electronic structure in ATK is based on DFT and an important ingredient in the calculations is the approximation used for the exchange–correlation functional. In addition, ATK can be used to calculate many different properties of the system, including electronic current, voltage drop,

transmission coefficients, electron density, etc. The results can then be exported to standard file formats so that they can be visualized in two or three dimensions, e.g. in VNL [80 – 81].

3.2.2.2. Virtual NanoLab

VNL gives you access to a powerful set of modeling tools for investigating nanoscale structures through a user-friendly graphical interface. The VNL software uses advanced software architecture and numerical methods to find solutions of the fundamental quantum mechanical equations describing the electronic properties of nanoscale objects by use of DFT and non-equilibrium green's functions (NEGFs) techniques. Based on the these techniques, VNL can simulate the detailed electronic structure and transport properties of molecules, bulk, crystals, nanotubes, and two-probe devices. The way you work with VNL is in many aspects similar to what you would do in an actual experiment:

- First we set up our system using either of the Bulk Builder, molecular builder, the Crystal Cupboard, or the Atomic Manipulator tools.
- After setting up our system (theoretical sample), we specify the details of the DFT method that should be applied to our system. We do this using either the Method Editor or the NanoLanguage Scripter tool.
- Once the DFT method has been defined, we select the physical properties that should be extracted from the calculation. We do this by using the NanoLanguage Scripter tool.
- The calculation is then performed by submitting the job to the Job Manager tool or executing it from the command line.

- Finally, we analyze and inspect the obtained data by using the Nanoscope and the Result Browser tools.

In short, VNL is designed to bridge experimental and computational approaches by offering a spectrum of useful tools for performing virtual experiments. The NanoLanguage scripts that are generated with VNL are performed with the ATK calculation engine. VNL provides you with several tools that assist you in defining the geometry of complex nanoscale systems [82].

Table 3.1: The VNL toolbar, which provides access to different stages of sample or device preparation and characterization, are summarized as follow:

Tool	Icon	Description
Crystal Cupboard		Database of bulk crystals
Bulk Builder		Build and construct bulk systems ready to be studied and analyzed with other VNL tools
NanoLanguage Scripter		Create complete calculation set-ups and store these as Nano-Language script
Method Editor		Predefine DFT and NEGF parameters for reuse in the Nano-Language Scripter when generating NanoLanguage scripts
Script Editor		Manually edit and extend NanoLanguage scripts constructed by the different set of VNL tools
Job Manager		Execute scripts using the ATK computation engine
Nanoscope		Visualize atomic geometries and calculated properties in 3-D

The numerical methods used in VNL are primarily based on first principles (ab-initio) and do not, in principle, require any input parameters regarding the quantum-

mechanical description of the atomic systems. Nevertheless, as is the case in most numerical simulations, a number of accuracy parameters must be specified to define the DFT and NEGF methods. Eventhough detailed knowledge of the input parameters is essential for users who wish complete control of their calculations and results, only a small subset of the parameters are really important, and it is not difficult to understand how they work.

3.2.3. Simulation Methods and Samples for a $Be_xZn_{1-x}Se$ alloy

Before we study the structural and electronic properties of a $Be_xZn_{1-x}Se$ alloy, we first have constructed a model of the atomic configuration we wish to investigate. Simulations of comparable accuracy on mixed alloys are seriously complicated by the necessity to treat large supercell, with a practical loss of any useful symmetry. The idea of constructing an alloy by taking a unit cell (cubic two atoms) and repeating it three dimensionally for the calculation of the electronic structure of the semiconductor alloy has been used for the binaries. The full structure optimization of cell parameters and internal coordinates is performed in all supercells prior to calculations of electronic, structural, DOS, and effect of pressure. Bulk $Be_xZn_{1-x}Se$ ternary alloy have studied in this work is modelled by repeating 3 x 3 x 3 FCC supercell conformation with 54 atoms per supercell since $2 \times 3^3 = 54$, two atoms per unit cell. These is done using bulk builder from the SIESTA software, at novel Be-composition (x) of 0, 0.33, 0.66, and 1, completely the full range of alloying is replicated and infinitely enlarge the system by repeating such a supercell. In the zinc blende-like structure, the atoms are tetrahedrally bonded so that each Se atom is surrounded by four cations (Be or Zn) as displayed in Figure 3.1. After modeling the sample using its standard atomic structure we drop it to the NanoLanguage Scripter

(NLS) and thus creating complete calculation script by using appropriate geometric optimization parameters and set-ups then we store this as NanoLanguage script and finally we execute the scripts using the ATK computation engine and standard command syntaxes. This would give us the configurationally optimized samples for different compositions. The resulting sample geometric xyz files are saved as python (.py) extension.

It is to be noted that for the compositions (x) of 0.33 and 0.66 we have replaced eight and seventeen Zn atoms from ZnSe, respectively, by Be atoms to get the desired concentrations. For the calculation of the structural properties, the crystal structures are optimized by force minimization (Quasi Newton method) in which the atoms are allowed to move towards the equilibrium positions. The different optimized simulational samples prepared for $Be_xZn_{1-x}Se$ ternary alloy have shown in Figure 3.1.

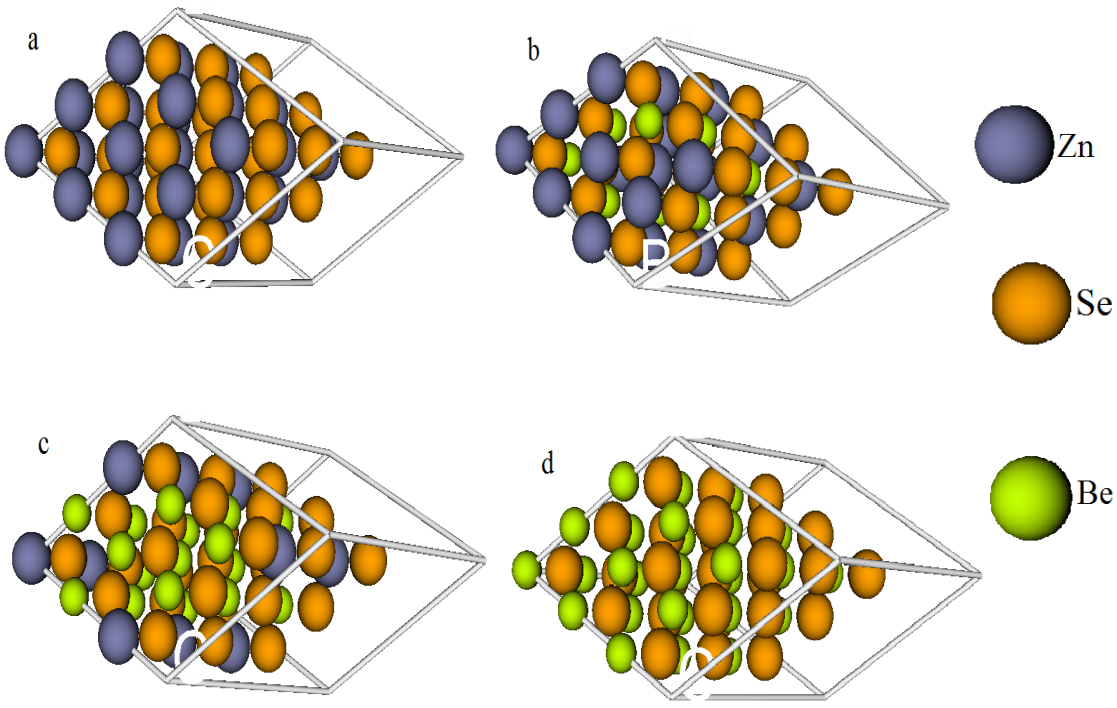

Figure 3.1: The schematic diagram of optimized structures of a $Be_xZn_{1-x}Se$ alloy at Be composition (x) of 0.0 (a), 0.33 (b), 0.66 (c), and 1.0 (d).

In order to carry out the study of structural and electronic properties of the samples, we have performed the following sets of simulational experiments-such as Total energy (TE), Band structures (BS), density of states (DOSs), etc. with the help of the following basic procedures performed the above sets of experiments. At first, we used the bulk builder tool to build the structure of the crystal. In the second step, python script of the samples prepared is loaded and dropped in to the NLS. The third step is setting up of DFT calculations and defining the physical properties that should be extracted from the calculations; these are accomplished by using the method tab in the NLS. In the NLS we set different parameters such as check file name, analysis, and method. The basic parameters used in the DFT rules are consistent for all the samples and they are summarized in the Table 3.2.

Table 3.2: Basic parameters used for our calculations for the ab-initio alloy modeling.

Parameters	**Bulk system**	**Values**
	Type	Double zeta polarized
	Energy shift	0.01 Rydberg
	Delta rinn	0.8
	V_o	40 Rydberg
	Split norm	0.15
	Radial sampling DR	0.001 Bohr
Brillouin Zone Integration	Number of K-points (A)	9
	Number of K-points (B)	9
	Number of K-points (C)	9
Eigen State Occupation	Left and right electrode electron temperature	300 Kelvin
Electrode voltage	Left Electrode	0
	Right Electrode	0
Electron density	Mesh Cut-off	200 Rydberg

Energy Counter Integral Parameters	Circle Points	30
	Integral lower bound	3 Rydberg
	Fermi Line Points	4
	Real Axis Infinitesimal	0.01 eV
	Real Axis Point Density	0.02 eV
Exchange Correlation Function	LDA-PZ (Perdew-Zunger functional)	
Iteration control	Tolerance	1e-003
	Criterion	Total Energy
	Maximum Steps	500
Iteration mixing	Quantity	Hamiltonian
	Diagonal Mixing Parameter	0.1
	Algorithm	Pulay
	History Steps	6
Two Central Integral Parameters	Points	1024
	Cut-off	2500 Rydberg

Finally the numerical calculation file (.nc) is created under the self-consistent tab. Under analysis tab of NLS we defined different quantities. As the program execution terminated normally, a complete calculation file is obtained from the log window and is stored for the further analysis.

CHAPTER FOUR

RESULTS AND DISCUSSIONS

In this section we will review the as obtained ab-initio results along with their suitable interpretation. We have used the ab-initio SIESTA code within the DFT, LDA approximation for exchange-correlation potential to investigate the structural and electronic properties of the cubic (ZB) structure of $Be_xZn_{1-x}Se$ ternary alloy. The alloy has been modeled at some selected novel Be-compositions (x) of the ordered structures described in terms of periodically repeated supercells. We have calculated the composition dependence of the structural and electrical properties like, lattice constants, the bulk modulus, pressure derivative, bandgaps, density of states, and the bowing parameters of a $Be_xZn_{1-x}Se$ ternary alloy at Be-composition (x) of 0.0, 0.33, 0.66, and 1.0. The ground state properties are important and fundamental to investigate the other properties. Therefore, we have performed and studied the structural optimization by calculating the total energies for different volumes around the equilibrium cell volume for these alloy systems as well as for the binary ZnSe and BeSe compounds.

4.1. Structural Properties of a $Be_xZn_{1-x}Se$ alloy

In this subsection, we calculate the structural properties for four values of x in the $Be_xZn_{1-x}Se$ system, although experimental values of the lattice constants are available only for x = 0.0 and x = 1.0 and thus the linearly interpolated (Vegard's law) values for x = 0.33 and 0.66 are used in present calculation. The zinc blende structure of $Be_xZn_{1-x}Se$ is characterized by the lattice constant (a). Consequently a series of lattice constants (a) are set to obtain the total energy E and the corresponding cell volume V.

Therefore, at the first stage of current work, the equilibrium value of the lattice constant is determined by calculating total energies of a $Be_xZn_{1-x}Se$ alloy at many different volumes around equilibrium. The minimization of the total energy with respect to the lattice constant in the ground state is performed for the Be composition (x) of 0.0, 0.33, 0.66, and 1.0. A more rigorous way to calculate bulk modulus (B) and its pressure derivative (B′) of ternary alloy $Be_xZn_{1-x}Se$ at each x is given by plot of total energy *versus* cell volume for a variety of cell volumes as showing Figure 4.1 along with a fitted curve to this plot. This means the calculated total energies at many different volumes around equilibrium are fitted by the Murnaghan Equation of state (Equation 1.15), thus the bulk modulus and its pressure derivatives for the alloy and the binary compounds are investigated.

A comparison of the total energy of the alloy $Be_xZn_{1-x}Se$ as a function of volume with their Murnaghan's fit for specific composition cases of x = 0, 0.33, 0.66, and 1 can be achieved by the data fits shown in Figures 4.1 (a) to 4.1 (d). The obtained values of equilibrium total energy (E_t), equilibrium lattice constants (a_{eq}), bulk modulus (B), and pressure derivative of the bulk modulus (B′) are listed together with the available experimental and theoretical data in Table 4.1.

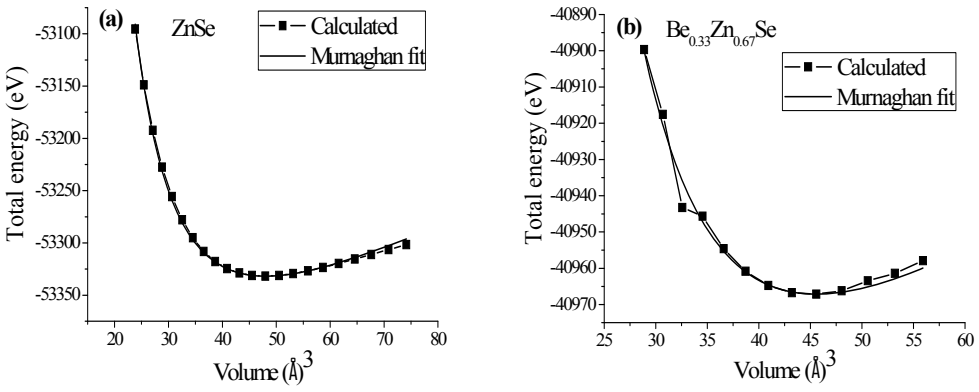

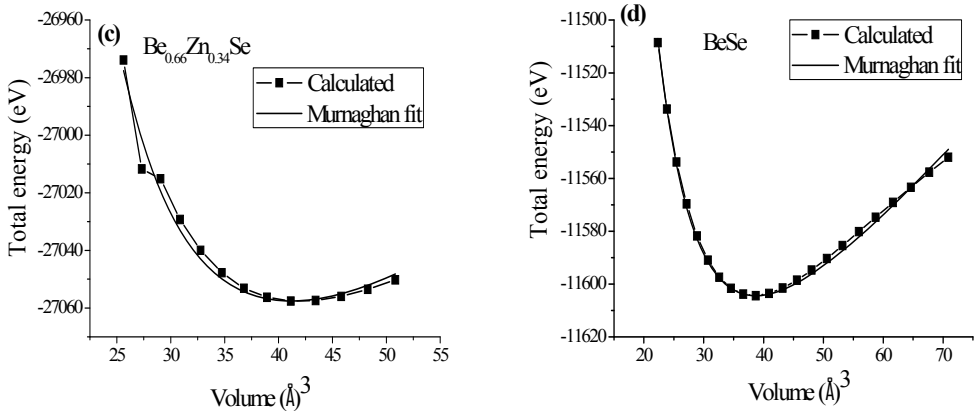

Figure 4.1: Calculated total energy as a function of volume. The line represents the fit of the Murnaghan equation of state: ZnSe (a), $Be_{0.33}Zn_{0.67}Se$ (b), $Be_{0.66}Zn_{0.34}Se$ (c), and BeSe (d).

Table 4.1: Calculated E_t, a_{eq}, B, and B′ for a $Be_xZn_{1-x}Se$ alloy. Available experimental and theoretical data from the literature are also included for comparison.

x		E_t (eV)	a_{eq} (Å)	B (GPa)	B′
0	Present	-53331.792	5.768	64.475	4.9
	Expt.	–	5.668 [15]	64.7 [14]	4.77 [14]
	Other calc.	–	5.7598 [45] 5.743 [15]	56.826 [15] 68.957 [14]	4.1298 [14]
0.33	Present	-40967.127	5.67	67	4.48
0.66	Present	-27057.580	5.48	72.531	4.01
1	Present	-11604.412	5.37	75.221	3.81
	Expt.	–	5.137 [14 - 15]	92.2 [14 - 15]	4 [14]
	Other calc.	–	5.098 [14] 5.183 [15]	74.569 [15] 79.8378 [14]	3.6665 [14]

The total energy determined here in Table 4.1 shows the robustness and the stability of the modeled alloy materials for the calculations of the ground state properties. It should be noted that, there is no available experimental or theoretical publication of

these values for the alloys of 0.33 and 0.66 to be compared with. Nonetheless, our results for the binary compounds are comparable with the reported theoretical investigations. However, we have a small over estimation of the lattice parameters and under estimation of the bulk modulus when we compare our results to the experimental data. This may possibly due to the use of the LDA. The LDA is the ground state theory, which cannot do very well in the excited state. The difference between our calculated 'a' and the available experimental data are 1.7% (ZnSe), 4.5% (BeSe), respectively. Nevertheless, our calculated structural parameters are in good agreement with those obtained by first principles methods within different approximations. The calculated bulk modulus values for ZnSe compound are in good agreement with the measured data, the differences between our calculated 'B' and the available experimental data is 0.34%, which ensure the reliability of the present first-principles computations. Generally speaking, the lattice parameters that we have estimated from the Vegard's expression as shown in Equation 1.1 are comparable with the DFT calculation for the respective compositions.

Figure 4.2; show the variation of the calculated equilibrium lattice constant *versus* concentration (x) for $Be_xZn_{1-x}Se$ alloy. We found that the configurationally averaged lattice constants from Vegard's law have only a small deviation, which are depicted by dotted curve as a linear variation of the lattice constant of alloys versus composition (x). However, from the literature survey it is tuned out that the violation of Vegard's law has been reported in semiconductor alloys both experimentally and theoretically [15].

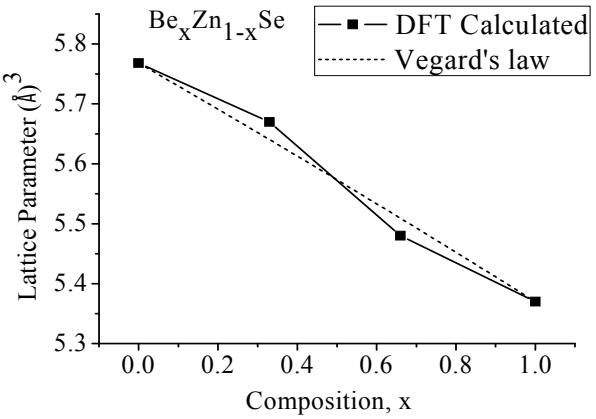

Figure 4.2: Composition dependence of the DFT calculated lattice constant (filled squares) of a $Be_xZn_{1-x}Se$ alloy compared with Vegard's law (dotted line).

Our calculated bowing turns out to be -0.017 Å as compared to the theoretical values of -0.04 Å [16]. The deviation from the Vegard's law should be mainly due to the lattice mismatch between BeSe and ZnSe compounds. The Vegard estimates show that the substitution of Zn by Be accompanied with monotonic decrease of the lattice parameter [16]. Similarly our calculated lattice constant of a $Be_xZn_{1-x}Se$ alloy decreases linearly with increasing x value according to Vegard's rule. However, our DFT calculated lattice constant *verses* composition curve shows a slight increase of the lattice constant at x value of 0.33 and also a slight decrease at x value of 0.66 (Figure 4.2) as compared with Vegard's law. This is due to the binary compounds (ZnSe and BeSe) bond-length distribution. Experimentally [13], it is found that (Be, Zn)Se alloy exhibits an unusually large contrast in the physical properties (bond stiffness and bond lengths) of its constituting bonds, leading to a uniquely well-resolved 1-bond→2-mode behaviour. From our DFT calculations also, we can recommend similar kind of proposition. At x value of 0.33 ZnSe have large bond length concentration. Therefore BeSe exhibits 1-bond→1-mode and it has less effect on lattice constant due to low bond concentrations, but ZnSe shows 1-bond→2-mode

behaviour which implies that one ZnSe bond, has larger value than its equilibrium value hence lattice constant increases. Similarly at x value of 0.66 the effect of BeSe is more prominent because BeSe has more bond concentration and shows 1-bond→2-mode behaviour, which implies 1-mode of BeSe should have smaller bond length in comparison to its equilibrium bond length hence the observed slight dip in the lattice constant.

Figure 4.3 shows the variation of the calculated bulk modulus *versus* concentration 'x' for a $Be_xZn_{1-x}Se$ alloy. To proceed further into analysis of the amount of deviation from the linear relation derived from the vegard like average configuration between the bulk modulus and the Be composition x, the curve (B *Vs* x) can be approximated by Equation 4.1 [61].

$$B(x) = xB_{BeSe} + (1-x)B_{ZnSe} - x(1-x)b \qquad (4.1)$$

It is obvious from Figure 4.3 that values of the bulk modulus increase with Be concentration, confirming the suggestion of Verie's prediction [14 – 15], which states that addition of beryllium to II–VI compounds improves their hardness and lifetime.

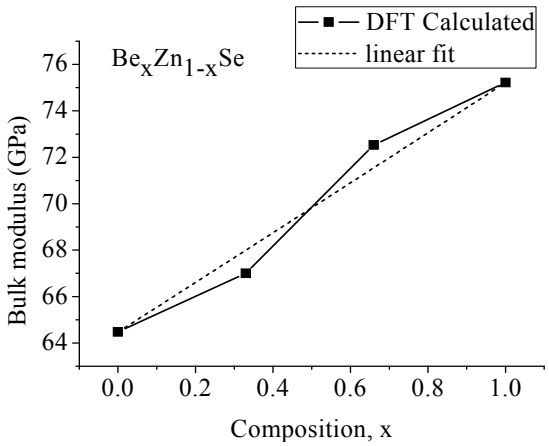

Figure 4.3: Composition dependence of the DFT calculated bulk modulus (filled squares) of a $Be_xZn_{1-x}Se$ alloy compared with the linear composition dependence prediction (dotted line) as estimated from the vegard like average configuration.

It is clear that a small deviation from the linear fit of alloy configuration is clearly visible also in Figure 4.3, which is responsible for the composition dependence of the bulk modulus for the $Be_xZn_{1-x}Se$ alloy. Our DFT calculated bowing turns out to be 0.096 GPa as compared to the other theoretical values of 1.177 Gpa [15]. Our calculated bulk modulus increases with Be composition (x) owing to the fact that BeSe is more tightly bound than ZnSe and results in a higher covalence, which respect to that for ZnSe. In similar fashion the calculated values of the bulk modulus decrease from BeSe to ZnSe, i.e. from the lower to the higher atomic number. This suggests that ZnSe is more compressive than BeSe. On the contrary, B′ monotonically decreased with increase in Be composition (x). Our DFT calculated bulk modulus *verses* composition curve shows the general trend of increase in the bulk modulus with increase in Be concentration. As shown in Figure 4.3 a slight decrease and increase of the bulk modulus at x = 0.33 and 0.66, respectively, is clearly visible as compared to the linear composition dependence, that is a dotted curve in Figure 4.3. The reason for these anomalies can be explained as follows. The bulk modulus of the material has an inverse relation with bond length and at x = 0.33 ZnSe have large bond concentrations than BeSe bond. Therefore, BeSe has less effect on bulk modulus due to lower bond concentrations, but ZnSe shows 1-bond→2-mode behaviour, which implies that one ZnSe bond has larger value than its equilibrium value, hence bulk modulus decreases. Similarly at x = 0.66 BeSe has more bond concentration and shows 1-bond→2-mode behaviour i.e. 1-mode of BeSe should have smaller bond length in comparison to its equilibrium bond length, hence increase in the bulk modulus. Thus our DFT calculated parameters of ground state modulii are in good agreement to experiments and other reported theoretical investigations, which give us much confidence to investigate the other properties of the alloy under pressure.

4.1.1. Pressure Effect on Structural Properties of ZnSe

In the $Be_xZn_{1-x}Se$ system, the constituent components ZnSe, BeSe exhibit contrasting properties, and their pressure-induced phase transformation also follows different paths. Pure ZnSe and BeSe both crystallize in the zinc blende (ZB) structure at low pressure and are known to transform to cubic rock salt (NaCl) and hexagonal NiAs structure, respectively, at high pressure. The phase transformation pressure increases linearly with Be composition (x) [12, 69]. In this work we computed the structural properties of ZnSe at high pressure by using the first-principle ab-initio SIESTA methods. Under this condition, the only information needed to determine the transition pressure is the total energy variation with volume. The structure of ZB phase of ZnSe is optimized at the pressure of zero (0) GPa. The calculated energy-volume data of the ZB and RS structures of ZnSe are shown in Figure 4.4.

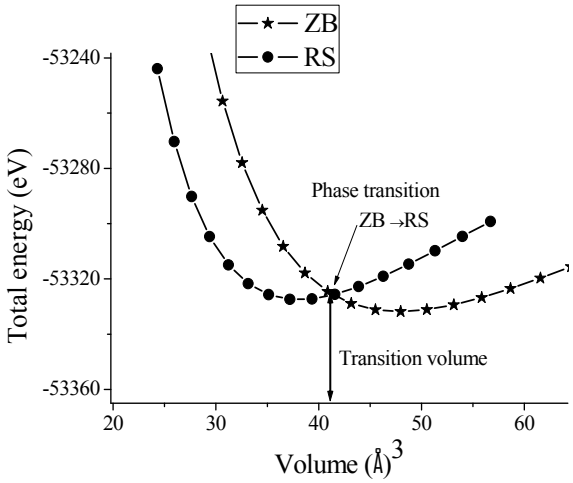

Figure 4.4: DFT calculated total energy *versus* volume for ZnSe in the phases of Zinc blend and rock salt.

The crossing of two curves indicates a phase transition between the two phases. Our calculation for ZnSe follows the transformation sequence of ZB to RS, which agrees

very well with the recently reported theoretical [69] as well as experimental [12] investigations. Our results show that a first-order phase transition from the ZB structure to the dense RS structure is at approximately 13.75 GPa. The ratio of the equilibrium volume of the RS structure to ZB structure of ZnSe is 0.78, which is in agreement with 0.84 of ref. [69]. In order to obtain the ground state properties of the two phases of ZnSe, we have fitted the total energy *versus* volume curves by Murnaghan's equation of state. The obtained values of a_{eq}, B, B′, E_t, and transition pressure (P_t) of ZB to RS phase of ZnSe compared with some available theoretical values and experimental data are listed in Table 4.2.

Table 4.2: The structural parameters of the two phases of ZnSe together with their transition pressure (P_t).

Phase		**a_{eq} (Å)**	**B (GPa)**	**B′**	**E_t (eV)**	**P_t (GPa)**
ZB	Present	5.768	64.475	4.9	-53331.792	13.75
	Expt.	5.668 [15]	64.7 [14]	4.77 [14]	–	13 [69] 11.8 [66]
	Other calc.	5.759 [45] 5.743 [15]	56.826 [15] 68.957 [14]	4.13 [14] 4.88 [14]	–	14, 15 [69] 13.5 [66]
RS	Present	5.299	80.0	3.665	-53327.405	–
	Expt.	5.299 [66]	104 [66]	–	–	–
	Other calc.	5.321[69] 5.304 [66]	100.75 [66]	–	–	–

Our calculated ZB to RS transformation pressure is slightly above experimentally observed transformation pressure of ref. [66], but is in good agreement with an experimental data of ref. [69] and also with other theoretical values (see Table 4.2). Our calculated lattice constant of the RS phase of ZnSe agrees very well with the experimental data [66]. Although a small energy difference can be shown in between

the ZB and RS structures. The obtained results show ZB structure is more stable than RS structure. That is, the energy state of ZB structure is the lowest one as compared to the RS structures, which is clearly visible in Figure 4.4 as the lower energy minima corresponding to ZB phase. Bulk modulus usually increases as the pressure is applied to the material for both the structures of RS and ZB. In addition, our calculated bulk modulus of RS structure is much higher than that of ZB structure of ZnSe. This is because the application of high pressure will certainly lead to shrinkage in volume and the total free energy of the system will also be affected from the equilibrium value. This is in addition to another competitive trend, application of high pressure will forces the atoms closer to each other with decreasing inter-atomic spacing between the atoms in the lattice. Consequently the bond exhibit the covalency nature, thus have larger bulk modulus. Generally, pressure is capable to drastically redistribute electron density, thus changing the nature of chemical bonds and converting semiconductors/insulators into metals and soft bonds into the stiffer ones. Moreover, the elastic constant of the materials at high pressures is essential in order to predict and understand the material's response, strength, mechanical stability, and phase transitions. Therefore, much more experimental and theoretical efforts are needed to further understand the pressure dependent properties of a $Be_xZn_{1-x}Se$ alloy.

4.2. Electronic Properties of a $Be_xZn_{1-x}Se$ alloy

In this sub section, we calculate the electronic properties for four values of x in the $Be_xZn_{1-x}Se$ ternary alloy at their respective DFT calculated equilibrium lattice constants. The essential ingredient in determining the electronic properties of solids is the energy distribution of the valence and conduction band electrons. Calculation of the bulk DOS spectra requires a very high degree of precision with the use of a fine

k–point mesh (high value of k–mesh) in the first Brillouin zone [83]. The band structure for the ordered material can be described only by the use of optimized supercell, although it is a more complicated calculation than for the normal unit cell, but it is the only way to incorporate novel crystalline effect present for the alloy. Systematic numerical errors can occur while integrating on sampled Brillouin zone of different cells size from 2 to 54 atoms. To overcome such errors, it will be more appropriate to use equivalent set of k–points as described by ref. [14]. In this work we have computed the electronic band structures and DOS spectra of a $Be_xZn_{1-x}Se$ alloy at novel Be composition (x) of 0.0, 0.33, 0.66, and 1.0.

4.2.1. Band Structures

We should begin with the actual definition of the bandgap, so we can understand what it is that we are actually aiming for. The bandgap is the minimum energy of an electronic excitation in which there is no interaction between the promoted electron and the hole that it leaves behind. In terms of the Kohn-Sham description of the system, the bandgap is usually taken to be the difference between the eigenvalues of the conduction band minimum and the valence band maximum, which are the bands positioned at just first two points on the either side of the zero point (E_f). The important applications of a $Be_xZn_{1-x}Se$ alloy in optical devices require the determination of the bandgap nature, which mean that either it is direct or indirect bandgap. The band structure calculations in the present work yield a direct gap (Γ–Γ) for ZnSe, while in the case of BeSe compound an indirect gap (Γ–X) has been determined. Hence, one can expect that the bandgap of the alloy should undergo a direct to indirect crossover at a certain value of x. For this purpose, we have calculated the direct and indirect bandgaps of the alloy at various concentrations. The

electronic band structures for the zinc blend form of a $Be_xZn_{1-x}Se$ alloy for the x = 0, 0.33, 0.66, and 1 compositions have been compiled in Figure 4.5.

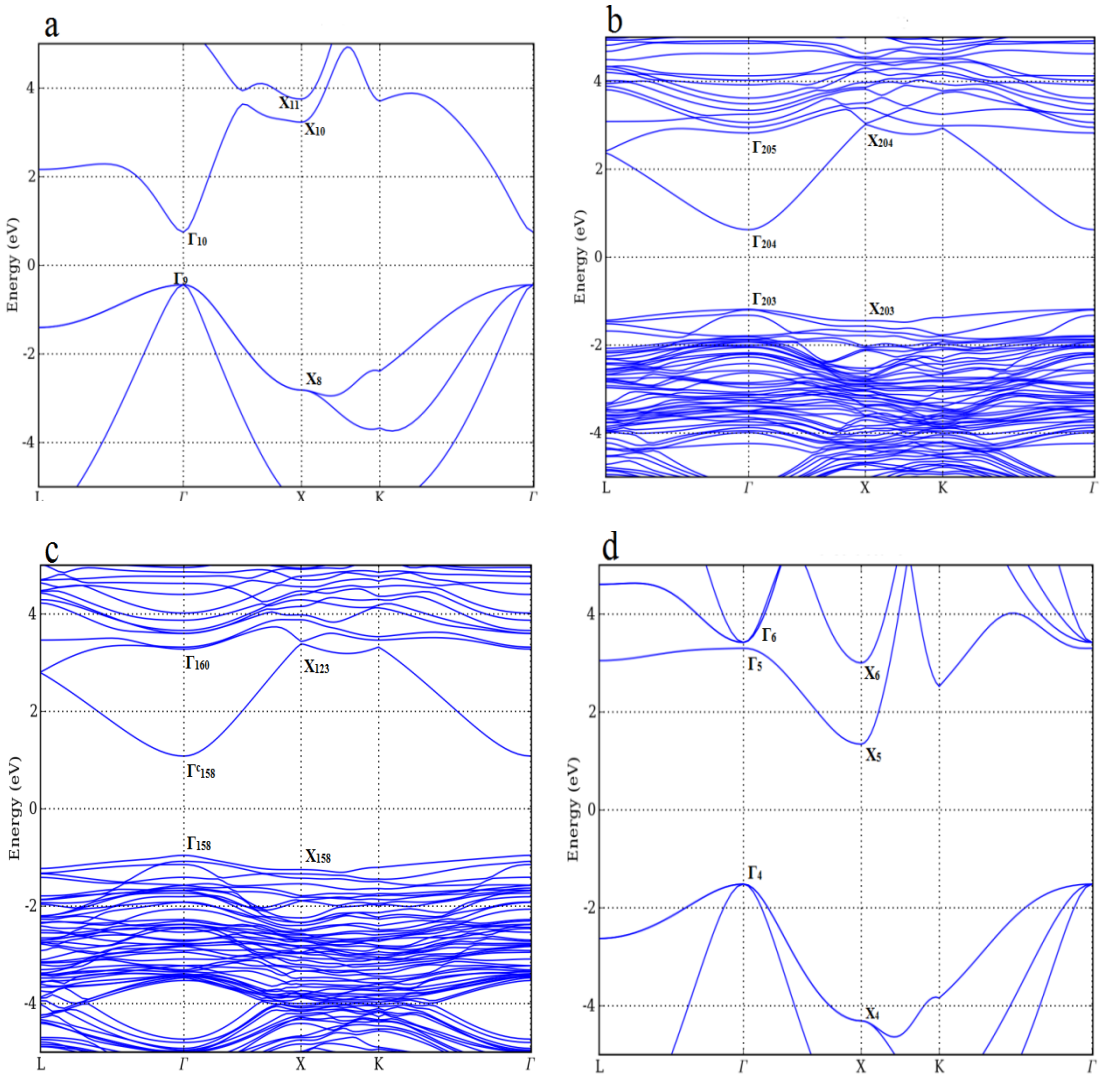

Figure 4.5: Band structures of a $Be_xZn_{1-x}Se$ alloy at Be concentrations (x) of 0.0 (a), 0.33 (b), 0.66 (c), and 1.0 (d).

Figure 4.5 shows the band structures at the as mentioned alloy concentrations. It is to be noted that the band structure in the Figures 4.5 (a) and (d) are obtained by using the primitive cell of two atoms for ZnSe and BeSe, respectively. While the band structure as shown in Figures 4.5 (b) and (c) are obtained by a well relaxed supercell of

3 x 3 x 3. Thus the numbers of atoms in these two DFT calculations are not similar. Hence, the numbers of band structure lines are increased by a factor of 27 in the two situations. However, it does not affect our present analysis as we are interested only in between the conduction band minima and the valence band maxima among the key symmetry k-points, while keeping band folding in consideration. Nevertheless, the 27 times increases in the number of band lines are definitely making one key observation more clear. If we look carefully at the total number of band lines below the Fermi level among the alloy concentrations of 33 % and 66 %, we can notice that the line density is more in 66 %, which is indicative of the promotion of the p-character of the alloy with doping.

From Figure 4.5, we determine the type of bandgap nature of the alloy, direct bandgap at composition of 0.0, 0.33, and 0.66 while in direct bandgap for BeSe. For composition of 0.0, 0.33, and 0.66 the valence band maximum and conduction band minimum occur at $\Gamma_9 \rightarrow \Gamma_{10}$, $\Gamma_{203} \rightarrow \Gamma_{204}$, and $\Gamma_{158} \rightarrow \Gamma^c_{158}$, respectively (see their value from Table 4.3). For BeSe, the valence band maximum (VBM) and the conduction band minimum (CBM) occur at the Γ_4 and X_5, respectively. From the obtained band structure curves of Figure 4.5 (a) and Figure 4.5 (d), we notice the important splitting in the valence bands at the X–point. This is owing to the fact that the split is more prominent in ZnSe (Figure 4.5 (a)), manifested by the large angle of branching. While in the BeSe as depicted in the Figure 4.5 (d), the branching is less prominent due to its low covalency of the bond. For BeSe less number of bands on the upper and lower side of Fermi level indicate the insulating nature of the BeSe, that is why we need the ZnSe–BeSe alloy for devices as ZnSe have good conductivity. We note that the fundamental gap (Γ–Γ) increases from Figure 4.5 (a) to Figure 4.5 (d) almost linearly

with increase of the Be composition. This is because an increasing replacement of Zn atoms by Be causes the atoms closer to each other (the smaller the volume per atom), the stronger character of the covalent bonds is observed. Thus due to the covalent character of Be, the cations state exhibit less orbital overlap extent and thus more sharing of electrons, which leads to the shrinking of the energy bands (valence band and conduction band) and thus the increase in the bandgap. The important features of the band structure along with the band indices of the important bands and their gaps in $Be_xZn_{1-x}Se$ alloy, as well as the theoretical and experimental gaps are given for a detailed comparison in Table 4.3.

Table 4.3: Direct (Γ–Γ) and indirect (Γ–X) bandgap energies of ZnSe and BeSe and their alloy at equilibrium volume, with their band structure (BS) energy.

Band gap energy (eV)				
x		**Γ–Γ**	**Γ–X**	BS energy (eV)
0	Present	1.1885 ($\Gamma_9 \rightarrow \Gamma_{10}$)	3.6689 ($\Gamma_9 \rightarrow X_{10}$)	-4260.3862
	Expt.	2.68 [15]	4.3 [14]	–
	Other calc.	1.11 [15] 1.176 [14]	3.07 [15] 2.805 [14]	–
0.33	Present	1.8082 ($\Gamma_{203} \rightarrow \Gamma_{204}$)	4.1992 ($\Gamma_{203} \rightarrow X_{204}$)	-3548.6596
0.66	Present	2.0373 ($\Gamma_{158} \rightarrow \Gamma^c_{158}$)	4.3410 ($\Gamma_{158} \rightarrow X_{123}$)	-2767.9464
1	Present	4.8154 ($\Gamma_4 \rightarrow \Gamma_5$)	2.8582 ($\Gamma_4 \rightarrow X_5$)	-1873.7729
	Expt.	5.15 [14 - 15]	4.0 [15] 4.5 [14]	–
	Other calc.	4.19 [15] 4.449 [14]	2.67 [15] 2.473 [14]	–

When comparing our results of the bandgap of ZnSe and BeSe with the reported theoretical investigations, ours are closer to the experimental results. Nevertheless,

our calculated bandgap is underestimated in comparison with the experimental results. This underestimation of the bandgaps is mainly due to the fact that the simple form of LDA does not take into account the quasi-particle self-energy correctly [14, 27], which make the LDA not sufficiently flexible to accurately reproduce both exchange-correlation energy and its charge derivative. It is also important to note that the density functional formalism is limited in its validity [27] and the band structures derived from it cannot be used directly for comparison with experiment. It is worthy to note that the difference found between our calculated bandgap and the experimental one does not affect the main goal of the present work, which is about the variation of the bandgap and not its absolute value. The calculated variation follows, indeed, the same trends, which are often observed experimentally. The error noticed is then only relative and not absolute. The variation of the direct Γ–Γ and indirect Γ–X bandgaps *versus* alloy composition is given in Figure 4.6.

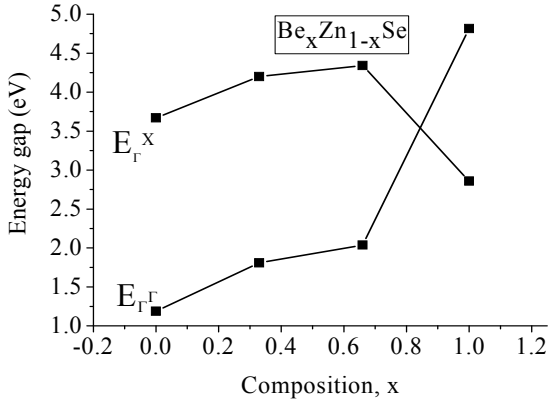

Figure 4.6: Composition dependence of the direct (Γ–Γ) and indirect (Γ–X) bandgaps in a $Be_xZn_{1-x}Se$ alloy.

A crossover between the direct and indirect bandgaps is located at a concentration of 0.84, which is close to the FP-LAPW value of 0.79 [15]. In Figure 4.6, we note that the fundamental gap (Γ–Γ) increases with Be composition. While the indirect gap (Γ–

X) decreases with Be composition. The total bowing parameter is calculated by fitting the nonlinear variation, with second order polynomial functions, of the calculated direct and indirect bandgaps *versus* concentration. The results are shown in Figure 4.7.

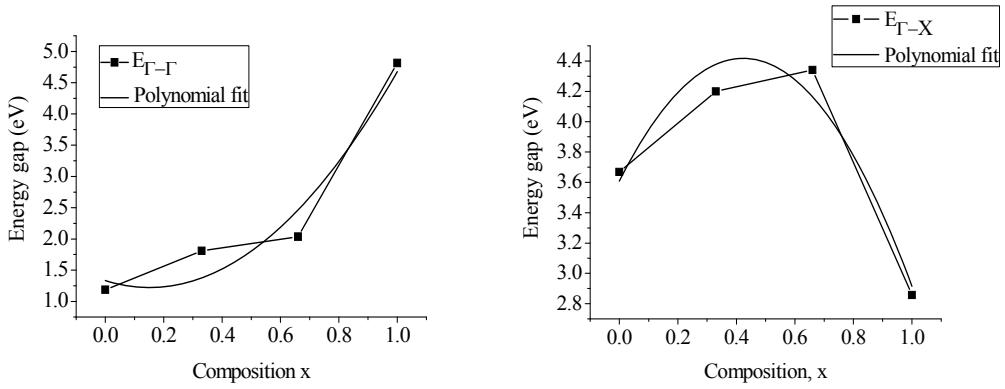

Figure 4.7: Polynomial fit of the direct (Γ–Γ) and indirect (Γ–X) bandgaps *verses* Be composition (x) of a $Be_xZn_{1-x}Se$ alloy.

Using the polynomial fit as shown in Figure 4.7, we found that our results obey the following variations:

$$E_{\Gamma-\Gamma} = 1.33 - 1.45x + 4.79x^2 \quad (4.2)$$

$$E_{\Gamma-X} = 3.61 + 3.82x - 4.51x^2 \quad (4.3)$$

It is shown from the above Equations that the variation of the direct (Γ–Γ) and indirect (Γ–X) bandgaps as a function concentration has a nonlinear behavior. Baaziz et al. [15] and Ameri et al. [14] also observed this nonlinear dependence on composition (x) by using ab-initio FP-LAPW and the FP-LMTO methods, respectively. It is interesting to note that the direct gap (Γ–Γ) *versus* concentration has a downward bowing with a value of 4.79, while the indirect gap (Γ–X) has an upward bowing of -4.51. The values of these bowings are much closed to those obtained by using the FP-LMTO method of 2.38 and -3.44 [14].

4.2.2. Origin of the Bandgap Bowing

Now we present details the origin of bowing in the energy gaps. As explained in Chapter one of our thesis, it has been recognized that mainly three effects contribute to the origin of bowing among the semiconducting alloys, *via* volume deformation (VD), charge exchange (CE), and the structural relaxation (SR) effects. In the present work, the overall bandgap bowing parameters for a $Be_xZn_{1-x}Se$ alloy has been calculated by the Equations of Bernard and Zunger. Using Equations 1.6, 1.8 and 1.10, the direct bandgap bowing coefficients 'b' for a $Be_xZn_{1-x}Se$ alloy are calculated at molar fractions of 0.33 and 0.66 and listed in Table 4.4.

Table 4.4: Decomposition of the direct bandgap bowing into VD, CE, and SR contributions (all values are in eV).

x	**b_{VD}**	**b_{CE}**	**b_{SR}**	**b**
0.33	3.25	-3.19	2.56	2.62
0.66	3.87	0.49	2.52	6.88

We note that from the obtained gap bowing a pronounced and positive structural relaxation contribution (b_{SR}) is registered. This is known to be relative to the large discrepancy between the atomic sizes of the alloyed cations, i.e., covalent radii; the Be ion (covalent radius of 0.97 Å) is much smaller compared with the Zn ion (1.22 Å) [13]. Therefore the change in bandgap is related to the structural effect and especially to the atomic bond relaxation, and thus exhibits large impact on the bowing of the $Be_xZn_{1-x}Se$ alloy. The smallest contribution to the gap bowing (b_{CE} sometimes negative) is attributed to the charge transfer. This is related to the electronegativity mismatch, which is very small between those of Be (1.57) and Zn atoms (1.65) [16]. For x = 0.33 the materials is still ionic in nature, therefore the CE effect is found to be

negative with a value of -3.19 eV. However, on increasing Be concentration the material becomes covalent hence electron sharing increases thus CE for composition (x) of 0.66 increases and becomes positive values of 0.49 eV. It is to be noted that bowing is always a constant parameter from Vegard's picture. This also shows that such mechanically contrasted alloy have multi-modal bond length, which manifested in the form of bowing variation. Therefore the bandgap bowing is mainly originated from the VD effect, which indicates towards the changes in the bandgaps of the bulk materials ZnSe and BeSe that are compressed and expand, respectively, from their equilibrium lattice constants to the intermediate alloy value of a(x) that is a clear deviation from the Vegard's rule, due to the large mismatch of the lattice constants between the bulk materials (7.4%) i.e. ZnSe and BeSe.

4.2.3. Density of States

The density of state (DOS) spectra plays a central role in many physical situations. The reason for this is quit simple; when one considers which states of a system are to be occupied, the energy of the states becomes the controlling factor. Thus DOS represents the number of electronics states in a band per unit energy per unit volume of the crystal. The DFT calculated DOS spectra for the $Be_xZn_{1-x}Se$ alloy are plotted in Figure 4.8 with the zero of energy corresponding to the Fermi level energy.

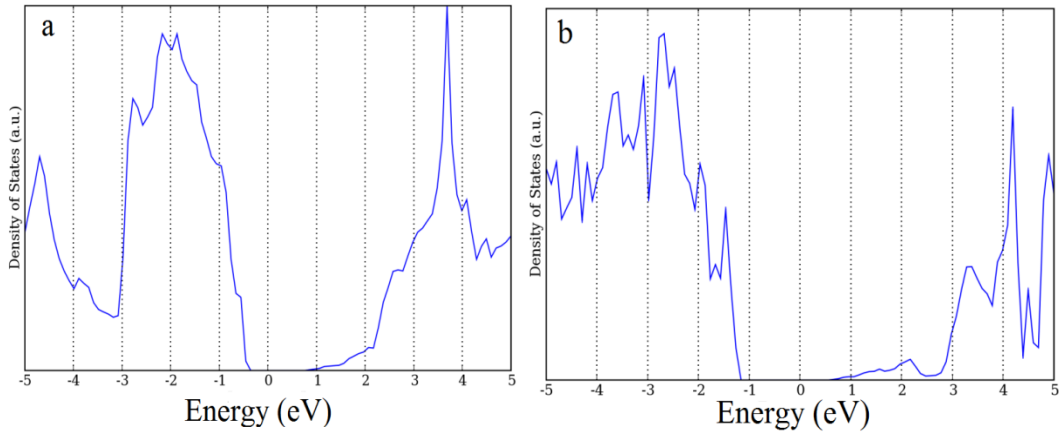

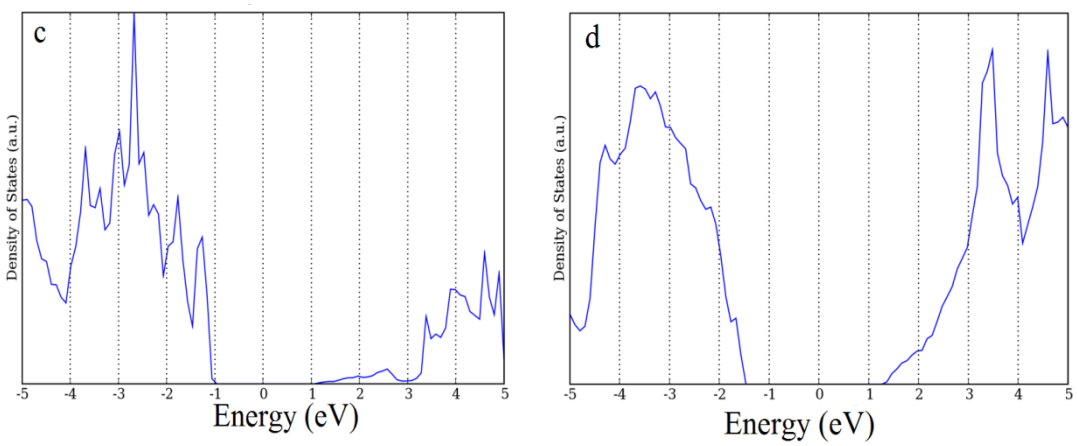

Figure 4.8: Calculated DOSs for a $Be_xZn_{1-x}Se$ alloy at Be concentrations (x) of 0.0 (a), 0.33 (b), 0.66 (c), and 1.0 (d)

The calculated DOS spectra (Figure 4.8) of the binary compounds ZnSe, BeSe, and their alloy show the type of conductivity of the material. We have found the p–type conduction character of the alloy. For ZnSe the DOS peak on the left and right side of Fermi level commences with the spectral positions of ~ -0.6 eV and ~ 0.9 eV, respectively. The value of gap in DOS, which is the gap in between first onset of electron density from the right and left side of the zero point, is found to be similar to the obtained gap energy from the band structure. It is clear from Figure 4.8 (a) DOS peak for the electrons on upper side of Fermi level shows step increase and reaches maximum value at ~ 3.4 eV. On the other hand, the DOS peak for the hole on left of Fermi level shows small electron density incremental, which are far away from the zero point. This explains the small p–type conductivity of the material. For BeSe the DOS peak on the left side of Fermi level commences from the spectral position of ~ -1.6 eV with a very sharp and large onset. On the other hand, the DOS peak for the electrons on upper of Fermi level starts from ~ 1.5 eV with very weak rise of electron density, which is indicative of strong p–type conductivity in the BeSe material.

For composition (x) value of 0.33 the DOS peak on the left side of Fermi level commences from the spectral position of ~ -1.2 eV and shows steep increase and reaches its maximum at ~ -3.8 eV with FWHM (full width half maxima) of -2.5 eV. On the other hand, the DOS peak for the electrons on upper of Fermi level starts from ~ 0.7 eV and shows very small values. Effectively DOS peak rises at ~ 2.8 eV with small FWHM of 2 eV. This explains the origin of strong p-type conductivity of the material. Similarly, for x value of 0.66 the DOS peak on the left side of Fermi level commences from the spectral position of ~ -1.1 eV, shows steep increase, and reaches its maximum at ~ -2.8 eV with FWHM of -2.5 eV. On the other hand, the DOS peak for the electrons on upper of Fermi level starts from ~ 1.0 eV and shows very small values. Effectively DOS peak rises at ~ 3.2 eV with small FWHM of 2 eV. This again explains the origin of strong p–type conductivity of the 0.66 material. In general, when the lowest conduction bands come closer at the X–point as the alloy is found to be Be rich. This may be a consequence of covalent character of bonding in Be rich alloy. Our calculations also show that the obtained values of gap in DOSs are found to be comparable with their corresponding band structure energies.

CHAPTER FIVE

CONCLUSIONS AND FUTURE OUTLOOKS

5.1. Conclusions

We have performed a systematic ab-initio DFT-LDA based modeling of cubic $Be_xZn_{1-x}Se$ ternary alloy and successfully performed the study of the effect of composition on the structural and electronic properties of the alloy as candidates for the design of blue–green laser diodes. We have calculated the composition dependence of the lattice constant, bulk modulus, pressure derivative, bandgap, and density of states by using the modelling of a geometrically relaxed unique supercell of 54 atoms. In this thesis, for the first time a $Be_xZn_{1-x}Se$ supercell is modelled for the novel concentrations (x) values of 0.33 and 0.66. A small deviation from Vegard's law with lattice constant bowing and the bulk modulus from linear concentration dependence as estimated from the Vegard like average configuration have been observed. This deviation is mainly due to the mismatch of the lattice parameter between BeSe and ZnSe compounds. The Murnaghan's fittings of the as obtained energy-volume relations show the bulk modulus for alloy increases with the Be concentration. Whereas the alloy lattice parameters are found to decrease with the Be concentration. The calculated band structures show a transition from direct to indirect band gap ($\Gamma\rightarrow\Gamma$) $\rightarrow$ ($\Gamma\rightarrow X$) at x = 0.84, which is in agreement with the FP-LAPW calculations. Nonlinear behaviour is observed on the composition dependence of the energy gap, with increasing of beryllium composition. In addition, the obtained values of gap in DOS spectra are found to be comparable with their corresponding band structure energies. The investigation of the origin of the bandgap bowing shows the VD effect, which accounts for the effect on band structures arising from the change of

equilibrium lattice constants, have larger contribution in the alloy tailored from the binary compounds having larger lattice mismatch. We have additionally predicted ZnSe compound transforms from ZB (FCC) at ambient pressure to the RS (NaCl) phase at high pressure. It is found that the phase transitions from the ZB structure to RS occur at 13.75 GPa. Finally, using the as obtained mechanical hardening, we can conclude that a $Be_xZn_{1-x}Se$ ternary alloy is useful in the realization of long-lifetime laser diodes by suitably adjusting their Be concentration.

5.2. Future Outlooks

1. It is possible to extend similar studies for other II-VI and III-V ternary alloys.
2. With the help of big supercell it is also possible to calculate the percolative formation of the 2-modal bond length behaviour.
3. Improvement of computing facilities can help in improvement of electronic structures and help in the study of effect of percolation on the transport properties of these devices.

REFERENCES

[1] Berghout A, Zaoui A, Hugel J. (2006) J Phys Cond Mat 18: 10365–10375.

[2] Grillo SE, Ducarroir M, Nadal M, Tournie E, Faurie JP. (2002) J Phys D Appl Phys 35: 3015–3020.

[3] Munjal N, Sharma V, Sharma G, Vyas V, Sharma BK, Lowther JE. (2011) Phys Scr 84: 035704–035713.

[4] Tewksbury SK. (1995) Microelectr Syst Research Cent 304: 293–6371.

[5] Swarnkar CB, PaliwaL U, Patel NN, Joshi KB. (2011) Bull Mater Sci 34: 499–506.

[6] Grillo SE, Ducarroir M, Nadal M, Tournie E, Faurie JP. (2002) J Phys D Appl Phys 35: 3015–3020.

[7] Kang JS, Park SH, Lee SG, Sohn SH. (1997) J Kor Phys Soc 30: 600–607.

[8] Miloua R, Miloua F, Arbaoui A, Kebbab Z, Achargui N, Benramdane N. (2008) Int Sc J Alt Ener Eco 62: 87–90.

[9] Hwang Y, Kim H, Um Y, Furdyna JK. (2007) J Kor Phys Soc 50: 858–861.

[10] Okereke NA, Ekpunobi AJ. (2011) J Non-Oxide Glasses 3: 31–36.

[11] Jia-Jin T, Guang-Fu J, Xiang-Rong C, Qing-Quan G. (2010) Commun Theor Phys 53: 1160–1166.

[12] Mazher J, Bhalerao GM, Polian A, Gauthier M, Itie JP, Baudelet F, Ganguli T, Deb SK, Pages O, Firszt F, Paszkowicz W. (2010) J Appl Phys 108: 083533–083539.

[13] Mazher J, Ganguli T, Polian A, Deb SK, Villain F, Pages O, Paszkowicz W, Firszt F. (2010) J App Phys 108: 083539–083546.

[14] Ameri M, Rached D, Rabah M, Khenata R, Benkhettou N, Bouhafs B, Maachou M. (2007) Mater Sci Semic Proc 10: 6–13.

[15] Baaziz H, Charifi Z, El Haj Hassan F, Hashemifar SJ, Akbarzadeh H. (2006) Phys Stat Sol (b) 243: 1296–1305.

[16] Berghout A, Zaoui A, Hugel J, Ferhat M. (2007) Phys Rev B 75: 205112–205120.

[17] Kuskovsky IL, Gu Y, Spanier JE, Herman IP, Neumark GF, Maksimov O, Zhou X, Tamargo MC, Smyntyna VA, Belous VM, Pasternak VA. (2004) J Phys Stud 8: 384–388.

[18] Kim BS, Kuskovsky IL, Tian C, Herman IP, Neumark GF, Guo SP, Tamargo MC. (2001) Appl Phys Lett 78: 4151–4153.

[19] Kuskovskylp IL, Gu Y, Vandervoort M, Tian C, Kim B, Herman IP, Neumark GF, Guo SP, Maksimov O, Tamargo MC. (2002) Phys Stat Sol (b) 229: 239–243.

[20] Plazaola F, Flyktman J, Saarinen K, Dobrzynski L, Firszt F, Legowski S, Meczynska H, Paszkowicz W, Reniewicz H. (2003) J Appl Phys 94:1647–1653.

[21] Desnica UV. (1998) Prog Cryst Growth Charact 36: 291–357.

[22] Maksimov O. (2005) Rev Adv Mater Sci 9: 178–183.

[23] Desnica UV. (1998) Vacuum 50: 463–471.

[24] Jaros M. (1985) Rep Prog Phys 48: 1091–1154.

[25] Mourad D, Czycholl G. (2012) Eur Phys J B 85: 153–162.

[26] Ilegems M, Pearson GL. (1975) Annu Rev Mater Sci 5: 345–371.

[27] Ameri M, Rached D, Rabah M, El Haj Hassan F, Khenata R, Doui-Aici M. (2008) Phys Stat Sol (b) 245: 106–113.

[28] Wronkowska AA, Wronkowski A, Skowronski L, Firszt F. (2010) Cryst Res Technol 45: 625–633.

[29] Oztas M, Bedir M, Bakkaloglu OF, Ormanci R. (2005) Acta Physica Polonica A 107: 525–534.

[30] Perna G, Capozzi V, Plantamura MC, Minafra A, Biagi PF, Pallara M, Orlando S, Marotta V, Giardini A. (2003) Appl Surf Sci 208: 582–588.

[31] Venkatachalam S, Nanjo H, Kawasaki K, Hayashi H, Ebina T, Mangalaraj D. (2007) Optoelect Mater Tech 6: 165–184.

[32] Lee H, Kim IY, Powell J, Aspnes DE, Lee S, Peiris F, Furdyna JK. (2000) J Kor Phys Soc 37: 1012–1016.

[33] Radoi R, de Andres M, Fernandez P, Piqueras J. (2004) Phys Stat Sol (a) 201: 3183–3187.

[34] Pages O, Ajjoun M, Bormann D, Chauvet C, Tournie E, Faurie JP, Gorochov O. (2002) J Appl Phys 91: 9187–9197.

[35] Murali KR, Thilakvathy K, Vasantha S, Ooomen R. (2008) Chalc Lett 5: 111–116.

[36] Murali KR, Dhanemozhi AC, John R. (2008) Chalc Lett 5: 277–280.

[37] Shakir M, Siddhartha, Bhagavannarayana G, Wahab MA. (2011) Chalc Lett 8: 435–440.

[38] Kumar P, Singh K. (2009) J Optoelect Biomed Mater 1: 59–69.

[39] Kasai J, Akimoto R, Hasama T, Ishikawa H, Fujisaki S, Tanaka S, Tsuji S. (2012) Phys Stat Sol C 9: 255–258.

[40] Philipose U, Saxena A, Ruda HE, Simpson PJ, Wang YQ, Kavanagh KL. (2008) Nanotech 19: 215715–215720.

[41] Mazher J, Shrivastav AK, Nandedkar RV, Pandey RK. (2004) Nanotech 15: 572–580.

[42] Guo SP, Luo Y, Lin W, Maksimov O, Tamargo MC, Kuskovsky I, Tian C, Neumark GF. (2000) J Crys Growth 208: 205–210.

[43] Mameri Z, Zaoui A, Belabbes A, Ferhat M. (2010) Mater Chem Phys 123: 343–346.

[44] Kumar S, Maurya TK, Auluck S. (2008) J Phys Cond Mat 20: 075205–075212.

[45] Chauvet C, Tournie E, Vennegues P, Faurie JP. (2000) J Electr Mater 29: 883–886.

[46] Basak T, Rao MN. (2010) AIP Conf Proc 1313: 202–204.

[47] Tsao JY. (2004) World of Compound Semiconductor.
URL: www.sandia.gov/~jytsao/WCS.pdf, Retrieved on May 30th 2012.

[48] Erbarut E. (2003) Sol Stat Commun 128:113–117.

[49] Postnikov AV, Pages O, Hugel J. (2004) Phys Rev B 71: 115206–115211.

[50] Mazher J, Ganguli T, Polian A, Deb SK, Pages O, Firszt F. (2009) J Phys Conf Ser 190: 012064–012067.

[51] Grein CH, Radtke RJ, Ehrenreich H, Chauvet C, Tournie E, Faurie JP. (2002) Sol Stat Commun 123: 209–212.

[52] Zakrzewski J, Firszt F, Legowski S, Meczynska H, Sekulska B, Szatkowski J, Paszkowicz W. (2000) J Microelectr 31: 821–824.

[53] Charifi Z, El Haj Hassan F, Baaziz H, Khosravizadeh Sh, Hashemifar SJ, Akbarzadeh H. (2005) J Phys Cond Mat 17: 7077–7088.

[54] Ameri1 M, Bouzouira N, Doui-Aici M, Khenata R, Yakoubi A, Abidri B, Moulay N, Maachou M. (2011) Mater Sci Applic 2: 749–757.

[55] Amrani B, Ahmed R, El Haj Hassan F. (2007) Computat Mater Sci 40: 66–72.

[56] Xu B, Su Y, Liu ZG, Zhang CH, Xia YD, Yin J, Xu Z, Ren WC, Xiang YH. (2011) Appl Phys Lett 98: 142112–142114.

[57] Scandolo S, Bernasconi M, Chiarotti GL, Focher P. (1995) Phys Rev Lett 74: 4015–4018.

[58] Bilge M, Kart SO, Kart HH, Cagin T. (2008) J Achieve Mater Manuf Eng 31: 29–34.

[59] Al-Douri Y, Reshak AH. (2011) Appl Phys A 104: 1159–1167.

[60] Bouamama Kh, Daoud K, Kassali K. (2005) Modelling Simul Mater Sci Eng 13: 1153–1162.

[61] Lachebi A, Sehil M, Abid H. (2009) J Turk Phys 33: 325–332.

[62] Gaudoinl R, Foulkes WMC, Rajagopal G. (2002) J Phys Cond Mat 14: 8787–8793.

[63] Kumar M. (1996) Phys Stat Sol (b) 196: 209–212.

[64] Zhang S, Li H, Li H, Zhou S, Cao X. (2007) J Phys Chem B 111: 1304–1309.

[65] McMahon MI, Nelmes RJ. (1996) Phys Stat Sol (b) 198: 389–402.

[66] Gangadharan R, Jayalakshmi V, Kalaiselvi J, Mohan S, Murugana R, Palanivel B. (2003) J Alloys and Compounds 359: 22–26.

[67] Munoz A, Rodriguez-Hernandez P, Mujica A. (1996) Phys Stat Sol (b) 198: 439–446.

[68] Cote M, Zakharov O, Rubio A, Cohen ML. (1997) Phys Rev B 55: 13025–13031.

[69] Jian-Dang L, Bin C, Jie Z, Li-Juan Z, Hui-Min W, Bang-Jiao Y. (2011) Chin Phys B 20: 108105–108109.

[70] Liang W, Chapman CT, Frisch MJ, Li X. (2010) J Chem Theory Comput 6: 352–3357.

[71] Meng YS., Dompablo MEA. (2009) Energy Environ Sci 2: 589–609.

[72] Peschel O, Schnell I, Czycholl G. (2005) Eur Phys J B 47: 369–378.

[73] Sutcliffe B. (2012) Int J Quantum Chem, DOI:10.1002/qua.24021.
URL: www.Q-Chem.org, Retrieved on June 13th 2012.

[74] Chen H, Zhou A. (2008) Numer Math Theor Meth Appl 1: 1–28.

[75] Romanowski Z. (2007) Acta Physica Polonica B 38: 3263–3286.

[76] Singh T. (2011) Dissertations University of Massachusetts – Amherst.
URL: www.scholarworks.umass.edu/open_access_dissertations/356/, Retrieved on May 29th 2012.

[77] Fiolhais C, Nogueira F, Marques M. (2003) Eds LNP 620, 1–55.
URL: www.springer.de, Retrieved on Jun 13th 2012.

[78] ATK (2011) Manual, Version 11.2.2.

URL: www.quantumwise.com/documents/manuals/atk-11.2.2-tutorial, Retrieved on March 9th 2012.

[79] Soler JM, Artacho E, Gale J.D, Garcia A, Junquera J, Ordejon P, Sanchez–Portal D. (2002) J Phys Cond Mat 14: 2745–2779.

[80] ATK (2008) Manual, Version 2008.10.

URL: www.quantumwise.com/documents/manuals/vnl-2008.10-tutorial, Retrieved on March 9th 2012.

[81] ATK (2006) Tutorial and Reference Guide, Version 2.0.

URL: www.quantumwise.com/manuals/ATK_2.0.4_Tutorial_and_Refere, Retrieved on March 20th 2012.

[82] VNL (2008) Tutorial, Version 2008.10.

URL: www.quantumwise.com/ documents/manuals/vnl-2008.10-tutorial, Retrieved on March 9th 2012.

[83] Abdiche A, Abid H, Riane R, Bouaza A. (2010) Acta Physica Polonica A 117: 921–927.

DECLARATION

This thesis is my original work and has not been presented for a degree in any other University, and that all sources of materials are used for the thesis have been duly acknowledged.

Name: Getasew Mulualem Zewdie

Signature: _____

Place and date of submission: Addis Ababa University, Addis Ababa, Ethiopia, 20/06/2012.

This thesis paper has been submitted for examination with my approval as a University advisor.

Name: Javed Mazher (Professor)

Signature _____